TP-VLQ
May 8, 1996
revised version May 31, 1996

Technical Proposal to build a Special Spectrometer covering Very Small Momentum Transfers

H1 Collaboration

supporting institutes

I. Physikalisches Institut der RWTH, Aachen, Germany
DESY, Hamburg, Germany
Institut für Hochenergiephysik der Universität, Heidelberg, Germany
Institute of Experimental Physics, Slovak Academy of Sciences, Košice, Slovak Republic
Institute of Physics, Czech Academy of Sciences, Praha, Czech Republic
Nuclear Center, Charles University, Praha, Czech Republic

Supporting Institutions

Ch. Berger, W. Braunschweig, O. Mang, H.-U. Martyn, P.-O. Meyer[1]
I. Physikalisches Institut der RWTH Aachen, Aachen, Germany

J. Bürger, NN
DESY, Hamburg, Germany

C. Brune, M. Keller, K. Meier, G. Schmidt, K. Schmitt, A. Stellberger, J. Stiewe, M. Weber
Institut für Hochenergiephysik der Universität Heidelberg, Heidelberg, Germany

D. Bruncko, J. Ferencei, F. Kriváň, R. Maraček, P. Murín, J. Špalek
Institute of Experimental Physics, Slovak Academy of Sciences, Košice, Slovak Republic

J. Cvach, I. Herynek, J. Hladký
Institute of Physics, Czech Academy of Sciences, Praha, Czech Republic

J. Žáček
Nuclear Center, Charles University, Praha, Czech Republic

Tecnical Support

S. Arbabi, W. Karpinski, C. Rente, O. Syben, F. Tenbusch, M. Toporowsky
I. Physikalisches Institut der RWTH, Aachen, Germany

[1] III. Physikalisches Institut der RWTH Aachen

1 Introduction

The total cross section for inelastic electron scattering

$$e + p \rightarrow e + X \tag{1}$$

depends at a given center of mass energy $\sqrt{s}$ of the $e\,p$ system on the two variables W^2 and Q^2. Here W is the invariant mass of the hadronic system X and Q^2 the negative mass squared of the virtual photon in the photo-absorption process

$$\gamma^* + p \rightarrow X \ . \tag{2}$$

At HERA these processes can be investigated over a huge range of Q^2, i. e. from $Q^2 \approx 0$ GeV^2 up to almost the kinematic limit s in one experimental setup. Above a certain threshold Q_0^2 (e. g. $Q_0^2 = 4$ GeV^2) inelastic electron scattering is known to be dominated by hard scattering processes and is well described by the QCD improved parton model. Somewhere below Q_0^2 the scenario changes drastically to the photo-production limit where the cross section is dominated by so called soft processes as in hadron hadron scattering.

It has become clear in recent years that the transition region between the photo-production and the deep inelastic scattering regime is particularly interesting. This region is currently not well accessible in the H1 detector. We propose the addition of a sophisticated special detector the **V**ery **L**ow $\mathbf{Q}^2$ spectrometer (VLQ) which covers the range $0.02 < Q^2 < 1$ GeV^2. It consists of two identical modules containing a tracker and a calorimeter with a surface area of approximately 9×12 cm^2. They are located at $z = -2.95$ m (front face of calorimeter) above and below the beam pipe[2]. It is interesting to note, that the VLQ and the SpaCal cover about the same area in the $\log x - \log Q^2$ plane, see figure 1.

The proposal is organized as follows. After a discussion of the physics goals (section 2) the general layout of the new spectrometer and a detailed discussion of its components and of the trigger and data acquisition system is presented in section 3. Possible background from synchrotron radiation is discussed in section 4. The calibration and alignment is described in section 5, followed by a presentation of the expected physics performance in section 6. The final section contains finances, responsibilities and time schedule.

2 Physics Motivation

In this section four topics are discussed which will benefit from the availability of an electron spectrometer covering the Q^2 range between 0.02 and 1 GeV^2. These investigations should lead to a deeper understanding of the interplay between soft and hard processes in electron proton scattering.

[2]In the H1 coordinate system the z-axis points along the direction of the incoming proton beam, x measures the horizontal and y the vertical direction.

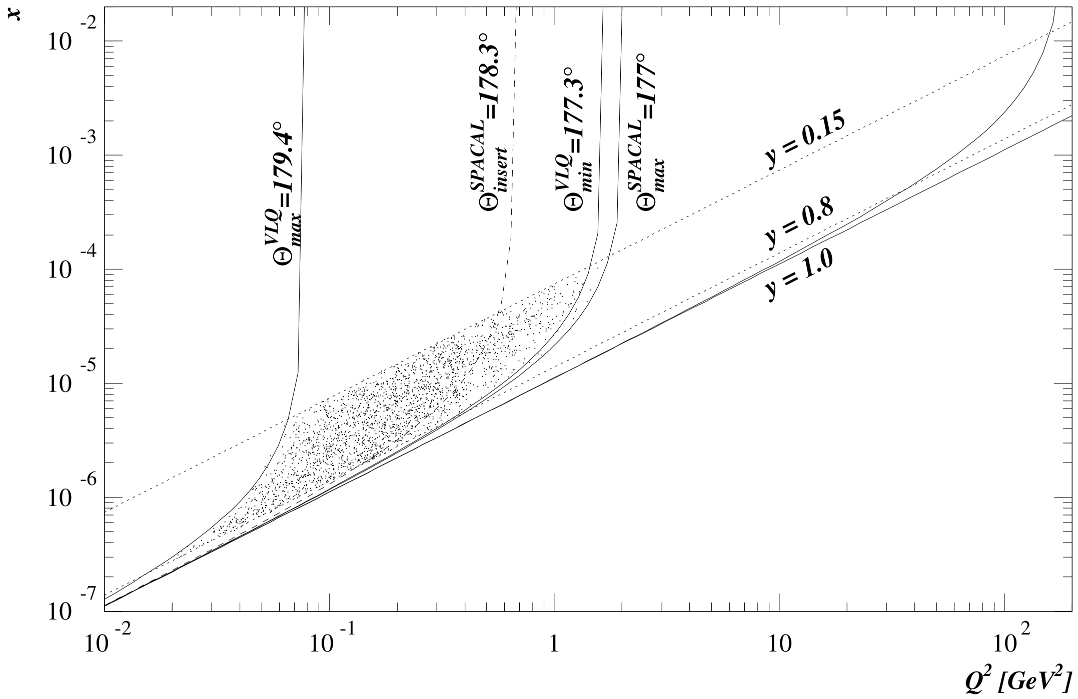

Figure 1: The VLQ and SpaCal acceptances in the $x - Q^2$ plane. The region bound by $\theta^{VLQ}_{min} = 177.3°$ and $\theta^{VLQ}_{max} = 179.4°$ indicates the VLQ acceptance. The acceptance of the SpaCal extends to $\theta^{SpaCal}_{max} = 177°$. The SpaCal insert closest to the beam pipe, extending to $\theta^{SpaCal}_{insert} = 178.3°$ (dashed curve), obscures part of the VLQ acceptance. The diagonals are lines of constant y. The points represent an event distribution in the VLQ with cuts of $0.15 < y < 0.80$.

2.1 Structure Function

One of the most prominent results of the HERA experiments is the strong increase of $F_2(x_B, Q^2)$ towards low values of the Bjorken variable $x_B = Q^2/(Q^2 + W^2)$. This increase is seen even at Q^2 values as low as 2 GeV^2. It can be accommodated in perturbative Quantum Chromo Dynamics (pQCD) using standard Altarelli–Parisi evolution techniques. The model of Glück, Reya and Vogt [1] (GRV) is particularly interesting because it predicts dynamically generated parton distributions starting from a valence quark input distribution at extremely low Q^2 values of ~ 0.3 GeV^2 (see fig 4 a)).

Converting F_2 into a total photo-absorption cross section via

$$\sigma_{tot}(\gamma^* p) = \frac{4\,\pi^2\,\alpha}{Q^2}\,F_2(W^2, Q^2) \qquad W^2 = Q^2\,(1-x)/x \tag{3}$$

the increase in F_2 at low x is translated into a strongly rising cross section as W increases. This is in contrast to the measured soft increase of the photo-production cross section, which shows the same slow increase with the center of mass energy as all other hadronic cross sections. In the Regge model of Donnachie and Landshoff [2] (DL) this behaviour is described by a universal pomeron trajectory.

The increase of F_2 at low x_B can be parametrized as $F_2 \sim x_B^{-\lambda}$ where the parameter λ depends on Q^2. Figure 2 shows a recent measurement of the H1 collaboration [4]. The photo-production limit corresponds to $\lambda = 0.08$. With the help of the VLQ it will be

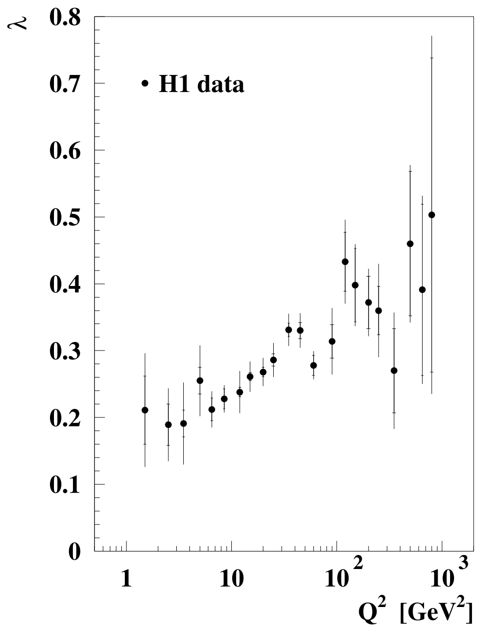

Figure 2: The parameter λ as a function of Q^2 which describes the increase of the structure function F_2 at small values of x_B (see text and ref. [4])

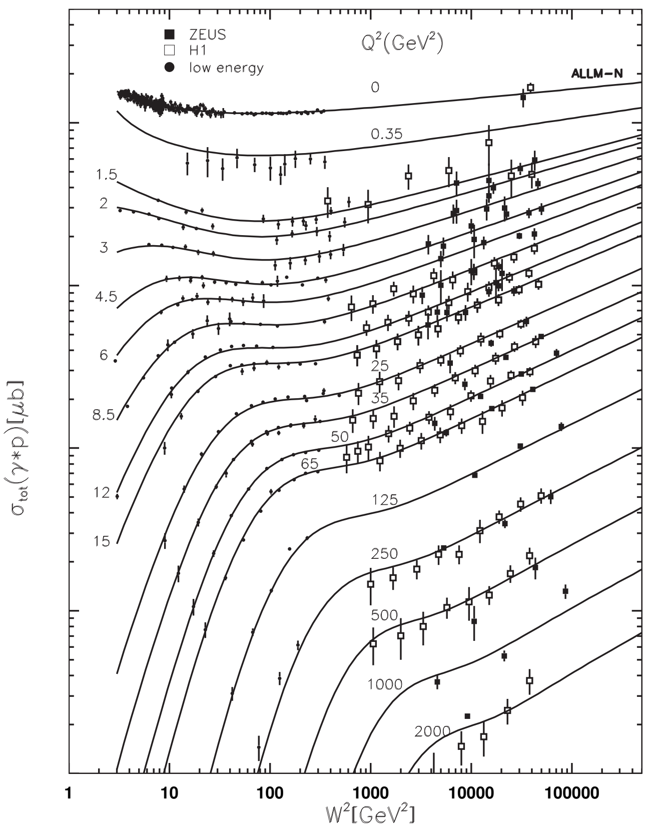

Figure 3: The total photo absorption cross section versus W^2 for various values of Q^2. The curves show parametrisations of a specific model [3].

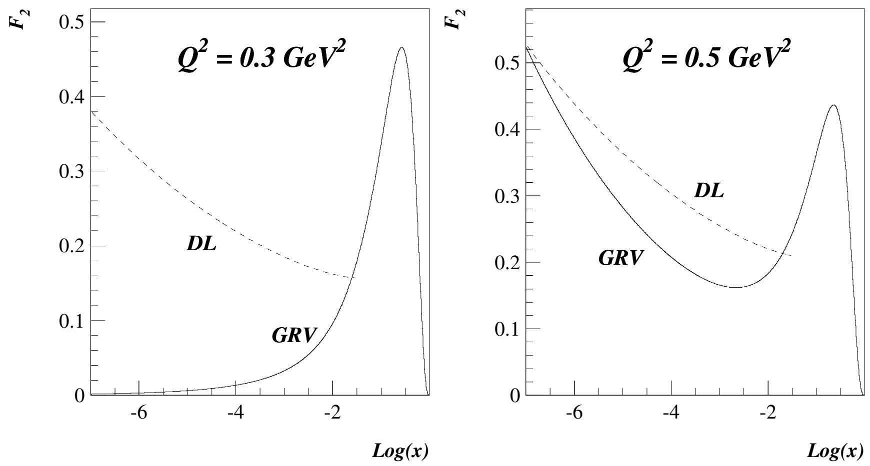

Figure 4: GRV [1] and DL [2] structure functions versus x at low values of Q^2

possible to investigate the transition from photo-production to finite values of the photon mass with high accuracy.

Figure 3 indicates our present knowledge of the cross section in the $W^2 - Q^2$ plane. The hole in the region $0.02 < Q^2 < 0.5$ GeV^2 and $W^2 > 200$ GeV^2 will be covered by the proposed addition to the H1 detector.

Figure 1 shows the density of events in the $x - Q^2$ plane. It has been generated with a mixture of both models, i.e. GRV for values of $Q^2 > 0.4$ GeV^2 and the result of Donnachie and Landshoff for $Q^2 < 0.4$ GeV^2. It is interesting to note that a naive extension of the GRV-model to $Q^2 = 0.5$ GeV^2 (figure 4 b)) is already close to the the Regge model which follows a power law in Q^2. The upper and lower diagonal lines in fig. 1 correspond to $y = 0.15$ and $y = 1$, with y being the relative energy loss of the electron in the proton rest frame. The two curves on the right hand side corresponding to electron polar angles of 177° and 152° indicate the acceptance of the SpaCal calorimeter.

2.2 Vector Meson Production

The cross section for the production of ρ meson by real photons is about 1000 times bigger than the corresponding J/ψ production cross section. This has always prevented a straightforward explanation in terms of vector meson dominance, because it leads to very different vector meson hadron scattering cross sections for ρ and J/ψ mesons. Electro-production experiments have shown that the difference decreases at larger values of Q^2. A recent H1 result [5] shows that at $Q^2 = 17$ GeV^2 the cross sections are practically equal and have a universal dependence on W^2. This fact is easily understood in pQCD where the cross section depends basically on the quark charge and the gluon content of the proton. Again the VLQ will allow to study the transition region between the two different production mechanisms and thus lead to a deeper understanding of vector meson production.

A detailed analysis will not only investigate the total production rate but also the helicity of the produced vector mesons. It has been shown that the ρ mesons are transversely polarized at $Q^2 = 0$ GeV^2 and longitudinally polarized at high values of Q^2. Note that the requirement of having an electron in the VLQ and both pions from ρ decay in the acceptance region of the backward silicon tracker leads to a visible cross section of ~ 2.5 nb.

2.3 Jet Production

Jet production in DIS is dominated by point-like $\gamma\, q$ interactions, e. g. photon gluon fusion, the generic Feynman diagram is shown in figure 5 a). In contrast at $Q^2 = 0$ GeV^2 jet production is dominated by resolved processes, see figure 5 b). Moreover final state interactions between the photon remnant and the proton remnant have to be taken into account. This leads to an underlying event structure.

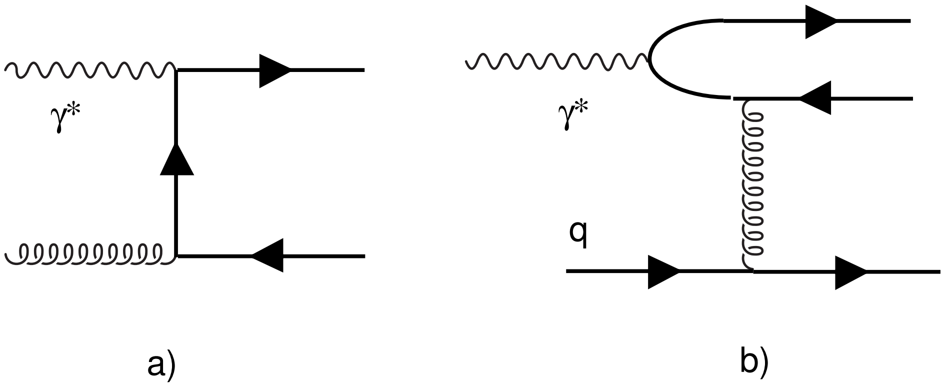

Figure 5: Feynman diagrams for direct and resolved photon parton interactions

At HERA jets in $\gamma\, p$ reactions have been used to investigate the partonic structure of the photon which is otherwise only accessible in deep inelastic $e\,\gamma$ scattering. Very little is known about the structure function F_2^γ of virtual photons. As can be seen from figure 5 b), this can be investigated using jet production. The virtual photon of mass Q^2 with $\Lambda^2 < Q^2 < p_T^2$ is probed by a quark at momentum scale p_T^2. Here Λ is the QCD scale parameter and p_T the transverse momentum of the jets in the photon proton center of mass system.

There exist QCD predictions [6, 7] for the Q^2, p_T^2 and x_B dependence of the virtual photon structure function. The VLQ will allow us to extend the presently accessible region by a large amount and to make detailed comparisons with theoretical calculations. Compared to deep inelastic electron photon scattering the analysis will be complicated by the fact that jets will not only be produced by the diagram in figure 5 b) but also by quark-gluon and gluon-gluon scattering. On the other hand these additional sources of jets will give access to the gluonic content of virtual photons.

2.4 Diffraction

In order to complete the physics discussion an example from diffractive physics is also included. At HERA it has been discovered that diffractive production mechanisms are responsible for a relatively high percentage ($\approx 10\%$) of the structure function measured in deep inelastic scattering up to Q^2 values of about 60 GeV^2. These reactions can be interpreted as deep inelastic electron *pomeron* ($e\,I\!\!P$) scattering. They are therefore used to determine the parton content of the pomeron. It has also been shown that diffractive dissociation in photo-production leads to final states containing jets.

Jet production in diffractive photo-production can be analyzed in terms of interactions between photons and partons inside the pomeron. In order to give a consistent picture the partonic content of the pomeron extracted from $e\,I\!\!P$ scattering and from photo-production of jets must agree. These experiments will eventually teach us if the extraction of parton densities in the pomeron in diffractive deep inelastic scattering can be used for the prediction of hard processes in diffractive hadron hadron scattering. It has e. g. been argued [8] that diffractive Higgs production at high energies might have less background problems than the standard channels. Certainly a VLQ covering the transition region between photo-production (where the diffractive cross section is dominated by soft processes) and deep inelastic scattering will be useful to investigate the connection between hard diffractive final states in these two different kinematic regimes.

3 The VLQ Detector System

3.1 Overall Layout and Environment

In order to meet the requirements outlined in the introduction the scattered electron has to be triggered and measured at polar scattering angles θ_e ranging from $\sim 178°$ to values as close as possible to 180°. Since at these scattering angles the $e\,p$ cross section is large, a full azimuthal acceptance is not necessary, so that exposure to direct synchrotron radiation in the horizontal plane of the accelerator can be avoided. The detector is of comparatively small size. Detection and triggering of QED Compton events (by measuring the photon and the electron in coincidence) requires two detectors back to back in azimuth. Such a system allows for the important in-situ energy calibration and alignment, and provides an additional luminosity measurement.

The VLQ detector will be mounted inside the iron yoke of H1, in front of the end-flange of the compensator solenoid. It consists of a high precision GaAs tracking system, a compact tungsten–scintillator sandwich calorimeter of a new ("energy projection") type, and a time-of-flight system for vetoing proton induced beam gas and beam wall events. The VLQ system comprises two identical subsystems mounted above and below the beam-line, respectively. A schematic view of the arrangement is shown in figure 6. Both half-systems can be moved apart from their positions close to the beam by means of precise moving mechanisms. The purpose of this feature is to protect the detectors (in particular the GaAs tracking system) from high background radiation during injection. In addition, the system can be moved during data taking if background conditions or trigger rates become prohibitive. Since cross sections for VLQ physics are large, not all luminosity needs to be recorded by the system.

The desired VLQ performance can only be reached if some modifications are made in the backward region of the H1 detector. These concern the beam pipe, the electromagnetic as well as the hadronic SpaCal calorimeter and the iron yoke.

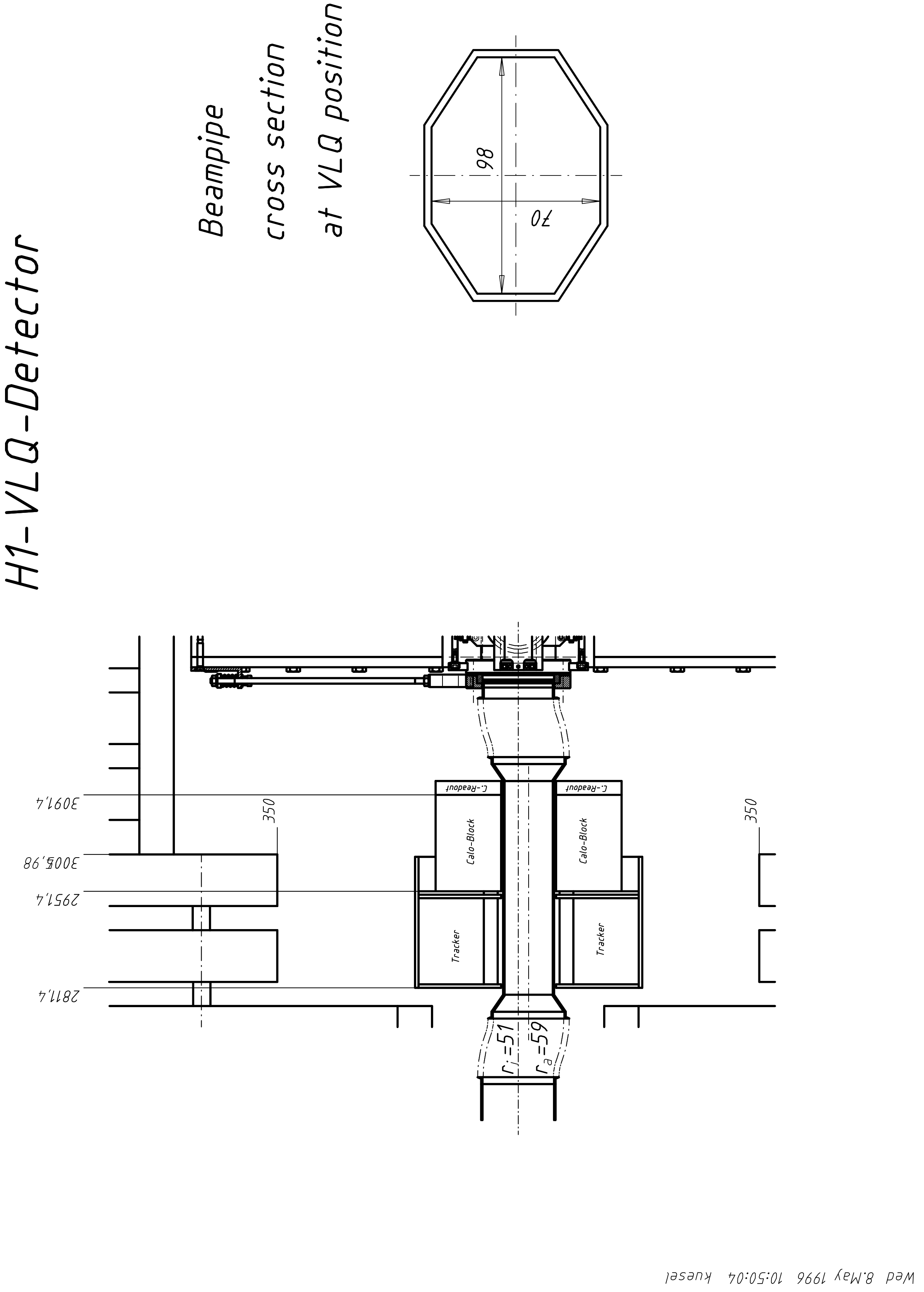

Figure 6: Schematic view along the beam-line showing the VLQ detector set up with the movable beam pipe. The bellow regions have a length of ∼80 mm each. For the general layout of the beam pipe see figure 7

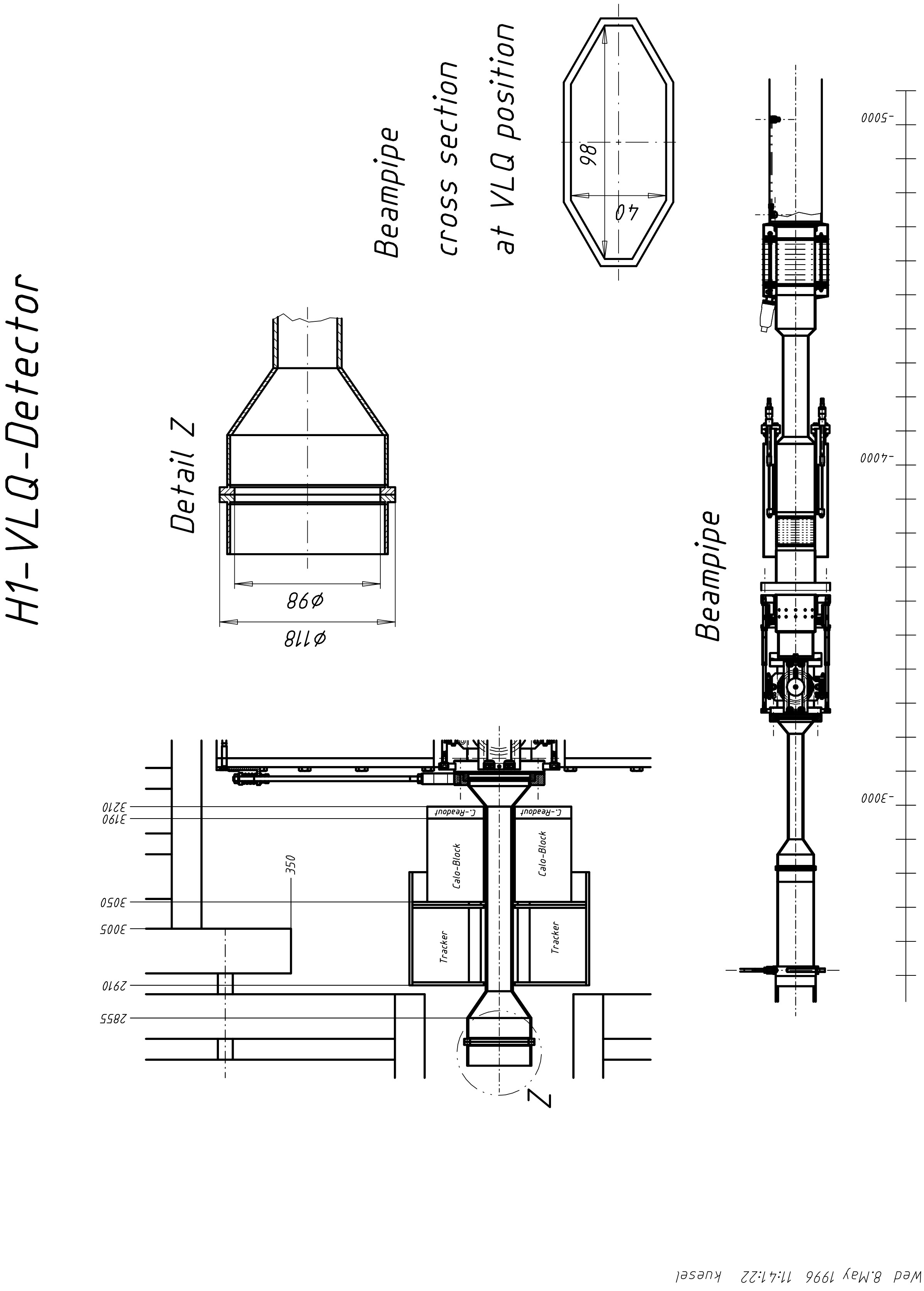

Figure 7: Schematic view along the beam-line showing the VLQ detector set up for the fall-back solution for the beam pipe

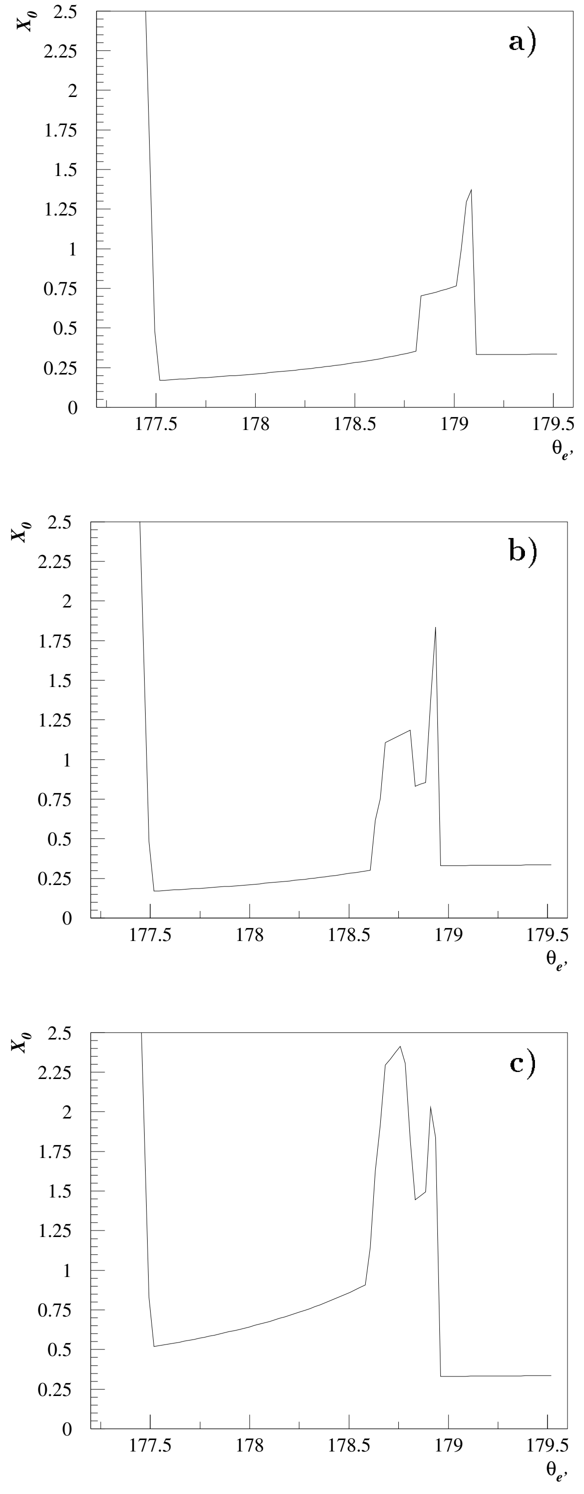

Figure 8: Material thickness in units of radiation lengths $X_\circ$ as a function of the scattering angle θ_e (fall-back solution). **a)** beam pipe made of carbon fiber, thickness 0.75 mm, inner radius $r_i = 45$ mm extending out to $z = -2600$ mm; **b)** beam pipe made of carbon fiber as for a), but with enlarged radius of $r_i = 52$ mm and thickness 1.25 mm in the region -2200 mm$\geq z \geq -2600$ mm; **c)** beam pipe made of aluminum with inner radii as for b) but with a thickness of 2 mm throughout. The calculations were done for the geometry of figure 7(fall-back solution). The distributions for the geometry of figure 6 (movable beam pipe with bellows) do not differ significantly.

- **Beam pipe.** Since the VLQ detector is located outside the main storage ring vacuum the wall thickness of the beam pipe is a crucial parameter for the performance of the VLQ spectrometer: within the angular acceptance its actual thickness as seen by the electrons and photons to be measured exceeds the geometrical thickness (in radial direction) by a factor $\sim$ 60. Therefore the beam pipe has to be as thin as possible. Our base-line design looks as follows:

  The existing beam pipe made of carbon fiber CFK (inner radius 45 mm, wall thickness 0.75 mm, thickness of the aluminum cladding inside 0.1 mm, extending in the backward region to $z = -1380$ mm) will be connected to a new CFK beam pipe with the same inner radius of 45 mm and wall thickness of 0.75 mm but with a thickness of the Al cladding on the inside of 0.3 mm, extending to $z \sim -2600$ mm. This part is followed by a transition from the CFK to a stainless steel (SS) beam pipe, with a cylindrical cross section and then by the dedicated, movable VLQ-beam pipe: it consists of a stainless steel part with a shallow octagonal cross section (height 70 mm, width 98 mm) connected at both ends to bellows which allow to move the pipe in the plane perpendicular to the beam, along any direction by ± 1.5 cm. A view along the beam line is shown in figure 6. We have adopted this scheme as the base line solution because it allows to adjust the beam pipe according to background conditions: Especially in the upper and lower wall of the beam pipe in the shallow region (see figure 6) the proton beam/beam halo might generate a severe background for the inner detectors of H1. We expect that with this design we can always position the beam pipe and the VLQ detectors such that the background is tolerable and that one VLQ spectrometer arm is located as close as $\sim$2.5 cm to the beam, and correspondingly the other arm at a distance of $\sim$5 cm from the beam. The details of the moving mechanics for the beam pipe are under investigation. The material thickness (given in units of radiation lengths X_0) as a function of the scattering angles is given in figure 8.

  With respect to a symmetrically positioned detector system this design has the additional advantage of an enlarged Q^2 acceptance, while keeping the possibility of the measurement of the QED Compton process. Critical issues are the following:

  1. The CFK-beam pipes are manufactured by several outside companies and experience has shown that very careful controlling of each production step is necessary. Enlarging the thickness of the inner aluminum cladding to 0.3 mm will diminish the risk of vacuum leaks. Nevertheless, as a fall-back solution an aluminum beam pipe will be made anyway. However, this would lead to an almost prohibitive amount of material in front of the detector, as can be seen in figure 8 c).

  2. Extending the beam pipe with the small inner radius of 45 mm into the region $-2200 \text{ mm} \geq z \geq -2600$ mm might cause problems with the direct synchrotron radiation fan being too close to the pipe wall and without the possibility of sufficient shielding by the collimator $C3$. Here we will rely on the experience to be gained during the 1996 running with the new relative positioning of beam/beam pipe/H1 detector as compared to 1995. A final decision has to be taken by late spring 1996. However, a beam pipe with an enlarged radius of 52 mm in the region $-2200 \text{ mm} \geq z \geq -2600$ mm would double the amount of material in a limited angular range ($\sim$ 15% of the acceptance) because the scattered electrons and photons would have to traverse the walls of both pipes.

The material thickness for this case is given in figure 8 b).

3. Because of RF interactions with the beams the bellow-sections (lengths 2×80 mm, inner radius 49 mm) need a special shielding at the inside. This is under investigation. If the proposed design turns out to be not feasible, we foresee as a fall-back solution for the beam pipe the scenario as sketched in figure 7. At $z \sim -2800$ mm the transition from the CFK to a stainless steel beam pipe (both with cylindrical cross sections) is followed by another transition from the cylindrical to a shallow octagonal cross section (height 40 mm, width 98 mm), which allow the VLQ detectors both to be moved as close as 2.5 cm to the beam, from above and from below.

   If required by unbearable background conditions, we propose to replace the shallow pipe by a pipe with larger height, which can be done in-situ. This operation, for which great expertise exists at DESY, has been discussed with the corresponding experts: it requires a short shut down (2-3 days) of Hera for opening/closing the detector, installing special jigs, cutting and removing the narrow pipe and welding the new one. Full restoration of the vacuum in the H1 interaction region requires about two weeks. This time could be shortened with vacuum pumps having larger power; the pumps are available at DESY, their installation would necessitate modifications (or rebuilding) of flanges in the region of the ring-vacuum valves (located at $z \sim \pm 15$ m from the interaction point). Investigations on this subject have started.

The proton beam-pickup antenna now housed in a SS-beam pipe in front of the compensator flange will move further into the backward direction and will be located inside the compensator in the region -4720 mm $\geq z \geq -5000$ mm (see figure 6). As has been confirmed by the experts concerned, this is technically possible and does not pose any physics problems w.r.t. the pickup signal.

- **SpaCal.** The special insert of the electromagnetic part (area around the beam-line: 162×162 mm^2) obscures the high Q^2 region of the VLQ (see figure 1). However, after discussions with the ELAN group and the Spacal calorimeter group we have decided to postpone our request for a modification of the SpaCal insert to the shut down 1997/1998. At that time a decision can be based on experiences concerning the performance of both the SpaCal and the VLQ detectors.

  The innermost upper and lower modules of the hadronic SpaCal calorimeter diminish the acceptance of the VLQ further, the effect (in addition to the above mentioned insert) not being very large. We propose to discuss at the end of 1996, based on the experience gained during 1996, the removal (not mdification) of the two modules during the shut down 1996/1997. This is considered to be a relatively easy and inexpensive operation; the mechanical stability requires the insertion of a thin support structure at the location of the lower module.

  Of course, the envisaged modification of the insert of the electromagnetic SpaCal during the shut down 1997/1998 makes only sense if the above mentioned hadronic modules are modified (or removed) as well.

- **Iron yoke.** In order to provide a reasonable lever arm for the tracking system (130 mm) and to allow for the vertical movement of the VLQ detectors a rectangular-shaped part ($\sim 350 \times 350$ mm^2) of two (for the case of the fall-back solution: one) of the 75 mm thick iron plates of the yoke have to be cut out symmetrically above

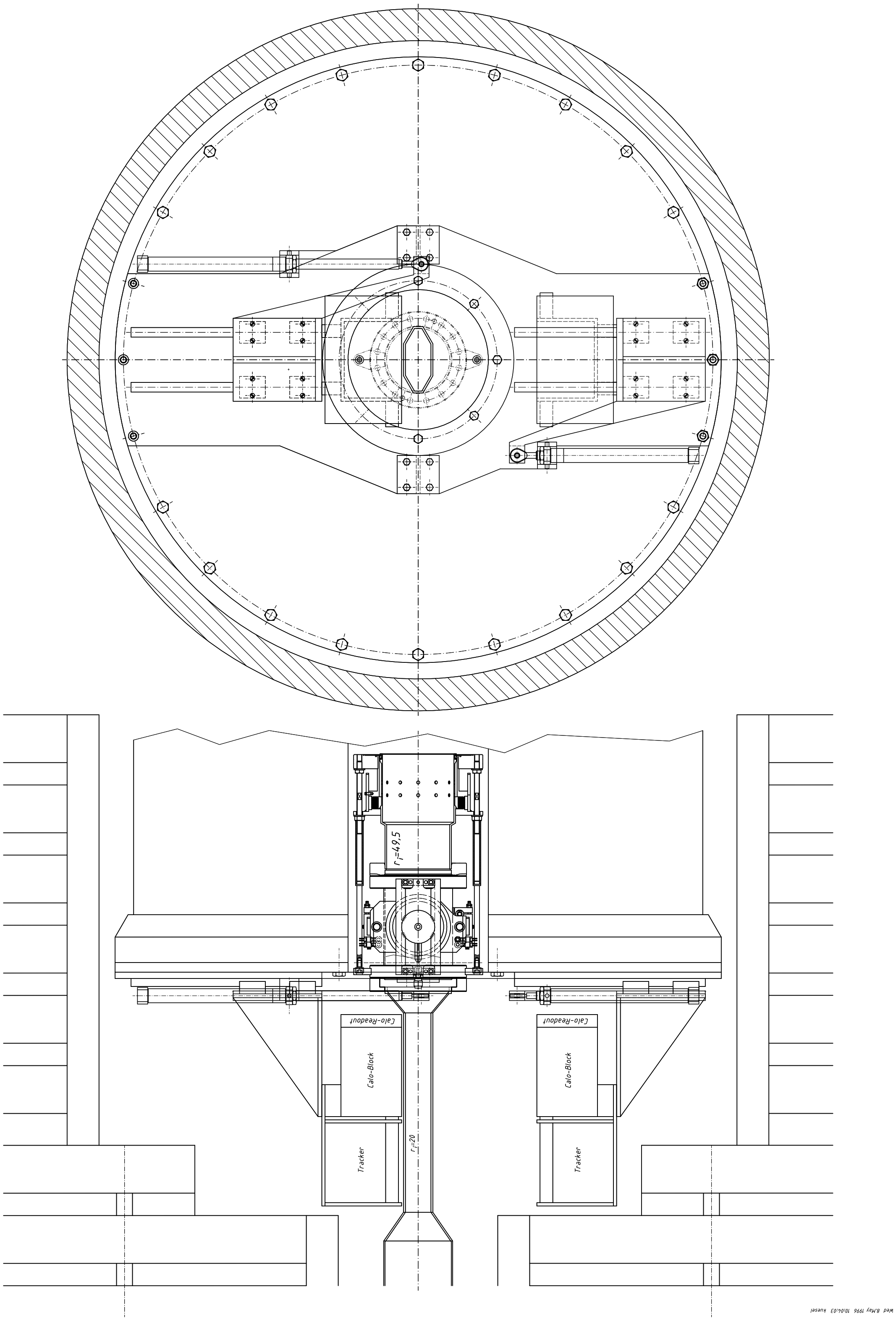

Figure 9: Schematic view of the moving mechanics for the VLQ detector modules and below the beam. Detailed investigations have shown that this is technically possible. The cut-out region is indicated in figure 6.

The moving mechanics for the VLQ detectors is based on a hydraulic system very similar to that used for the FPS (forward proton spectrometer) of H1. This includes also the controls and the connection to the H1–CDAQ. The complete detector together with the moving mechanics will be assembled above ground and will be transferred as a whole to H1 and fixed to the end-flange of the compensator magnet. A sketch of the arrangement is shown in figure 9. The number of cables to be guided from the detector to the various control and readout stations of H1 is very small. In total 6 – 8 multi-conductor cables will be needed; they can be installed prior to the detector installation at the earliest possible date during the shut down. The detector installation will be easy and fast (about 1-2 days).

3.2 The Energy Projection Calorimeter

3.2.1 Basic Design Ideas

The calorimeter is designed to detect electrons scattered off protons at very low values of Q^2. It will consist of two identical modules mounted above and below the beam line. The range of electron energies extends from a few GeV up to the beam energy. Due to the limited space available, the calorimeter must be extremely compact in order to ensure satisfactory longitudinal and lateral containment of the electromagnetic shower. We are aiming for energy resolution of a few (3 – 4) % at 30 GeV, and a spatial resolution of the order of 1 mm. Longitudinal and lateral containment will, however, not be perfect. Longitudinal leakage contributes to the so called “constant term” of the energy resolution. Lateral leakage degrades the energy measurement at the edge of the calorimeter. To correct for these effects, a precise knowledge of the shower position and its influence on the energy calibration is mandatory.

These requirements, together with the need to keep the number of electronic readout channels reasonably low, are met by a novel type of calorimeter, based on the well established sandwich–calorimeter: The “Energy Projection Calorimeter (EPC)”. The principles of such a calorimeter are sketched in figure 10. There is a twofold projective readout: One layer of active material is segmented in narrow vertical scintillator bars, the next one in horizontal scintillator bars, and so on. Each scintillator is read out at both ends via wavelength shifters extending over the entire length of the calorimeter, thus integrating the light from the vertical and horizontal scintillator bars, respectively. Two projections of the lateral shower profile are measured, from which the x and y coordinates of the impact point can be reconstructed. Compactness of the EPC is achieved by using tungsten as the passive medium.

The wavelength shifter (WLS) bars are read out by photodiodes (PD), which is the only realistic choice, as e.g. photomultiplier tubes would occupy far too much space. The ensemble of scintillator, WLS and photodiode can be customized to optimize the optical properties of each element (wavelength at maximum emission, quantum efficiency, etc.).

The readout scheme delivers four measurements of the shower profile, two horizontal and two vertical projections. Figure 11 shows the projections from a simulation study

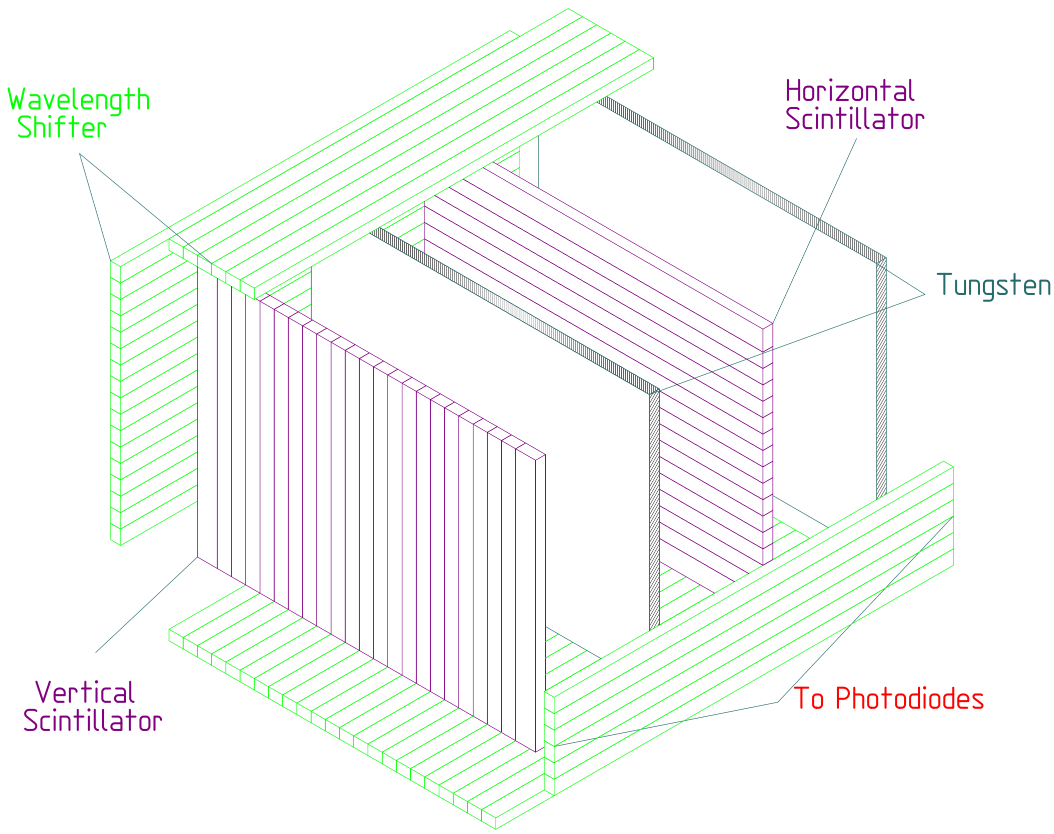

Figure 10: Exploded view of the EPC structure

where both readout sides are already summed. The four–projection readout offers several advantages: One gets redundant information for shower reconstruction and energy measurement and one has an effective means to overcome the so called "single diode" or "nuclear counter" effect. This is caused by photo-absorption of e.g. a synchrotron radiation photon in the depletion zone of a PD, and the subsequent charge liberation in the depletion layer through the photo effect. This effect is especially dangerous in the trigger circuit, while it can rather easily be corrected in the offline analysis. Due to the fourfold redundancy, however, the trigger can be adjusted such that a "single diode" event will not fire.

3.2.2 Mechanical Layout

Overview The active structure of the calorimeter is drawn in figure 12. The elementary cell of the calorimeter is a tungsten plate of 2.5 mm thickness, followed by a segmented plate of 3 mm plastic scintillator. The segmentation will be alternately horizontal and vertical. This elementary pattern is repeated 23 times, plus one additional layer of scintillator in front of the first tungsten plate. The front plate of the stainless steel housing (thickness = 0.5 cm) serves as the first absorption layer of the calorimeter. The total depth of the active structure in beam direction is 14 cm, corresponding to 16.7 radiation lengths, including the front plate and an air gap where the readout electronics is mounted.

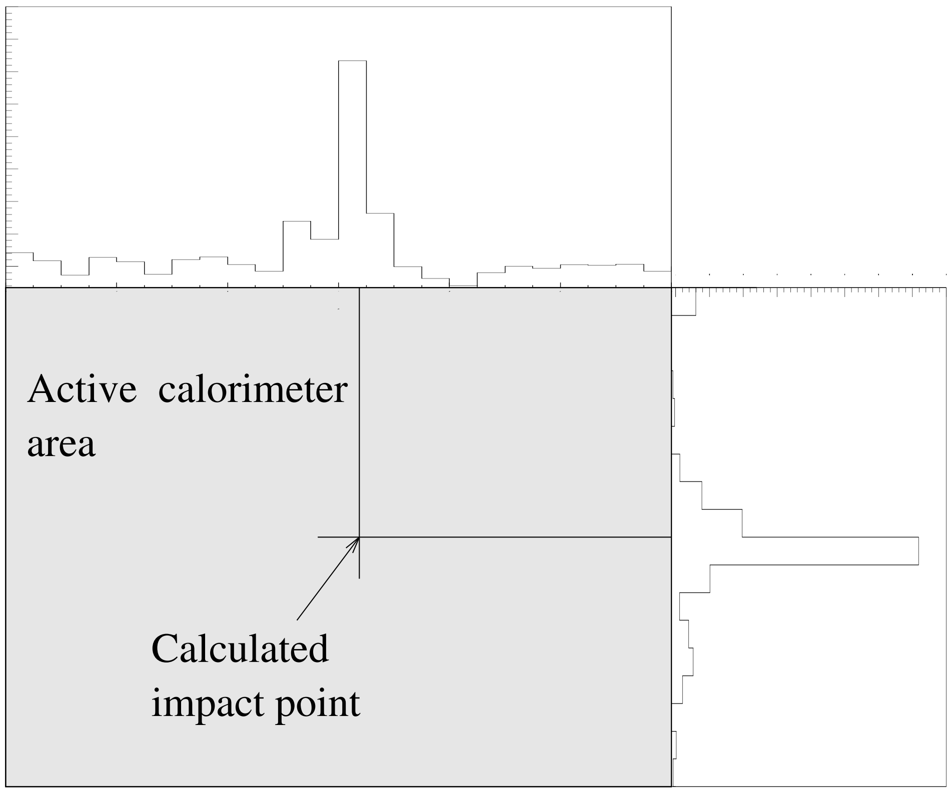

Figure 11: The two projections of the shower profile extracted from a simulation of 5 GeV electrons. The histograms contain the electronics noise. The reconstructed impact point is also shown.

The lateral dimensions of the calorimeter are $9 \times 12\,\mathrm{cm}^2$. The width of the scintillators is chosen to be 5 mm, leading to a segmentation into 18 vertical and 24 horizontal slabs.

The scintillators need protection against light leakage to prevent cross talk, which will be achieved by wrapping the bars in white paper or by inserting paper sheets or strips between adjacent scintillator bars and between scintillators and tungsten plates. Scintillator and WLS bars are kept at a well defined distance by inserting Nylon threads of 0.3 mm thickness between adjacent surfaces. This results in a stable optical coupling between scintillator and WLS and maintains total reflection in the scintillators and wavelength shifters. Photodiodes will be arranged in arrays matching the dimensions of the WLS exit surfaces and will be glued to them.

An entire calorimeter module will be kept in a stainless steel housing whose back plane will be fixed to the moving mechanics.

Details of the Mechanical Design The mechanical structure of the calorimeter can be seen in figure 13 (front view) and figure 14 (side view). The fully assembled calorimeter will be housed in a stainless steel box with dimensions $120 \times 140 \times 150\,\mathrm{mm}^3$.

The active structure is mounted in a housing which holds the wavelength shifters. To prevent damage of the wavelength shifters due to mechanical stress caused by the weight of the active structure, it is fixed by guiding rails screwed to the outer housing (see figures

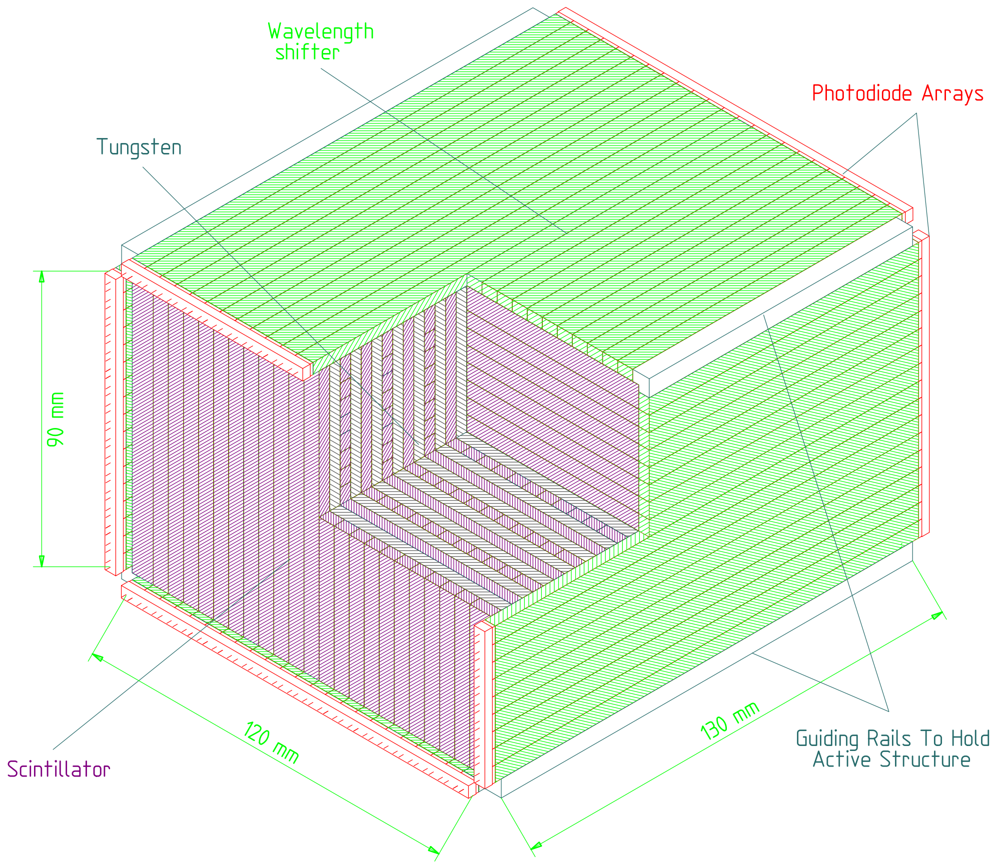

Figure 12: Active calorimeter structure of the EPC

12, 13 and 14). The edges of the tungsten plates fit exactly into the rails and are thus carried by them. The first and last scintillator planes are screwed to a support frame (thickness 2 mm) and then the front and back surfaces of the guiding rail. This plate has a rectangular hole in the middle in which the electronics fits (see figure 13). The support frames serve also to fix the Nylon threads, shown in the expanded view of figure 15. The threads are fixed laterally by little notches in the support frame. The connection between front plate and threads is provided by glue.

The mechanical arrangement of the electronics can be seen in figure 14. There are three PCB's (Printed Circuit Boards), mounted on top, in front and on the back of the active structure. The front and back PCB's carry the preamplifiers for the photodiodes. The photodiodes are arranged in linear arrays which fit exactly on the readout structure. The diode arrays are glued directly on the wavelength shifters. The connection of the photodiodes are soldered on the PCB's. The top PCB carries summing amplifiers and line drivers to transmit the signals to the readout electronics, located $\sim$30 m away.

The power dissipation of the electronics will be about 70 W. Since the electronics is mounted in a closed housing, cooling has to be foreseen. This is done by a flow of cold nitrogen, provided by the experiment. The nitrogen inlets and outlets are shown in figures 13 and 14.

A summary of mechanical parameters of the EPC is given in table 1.

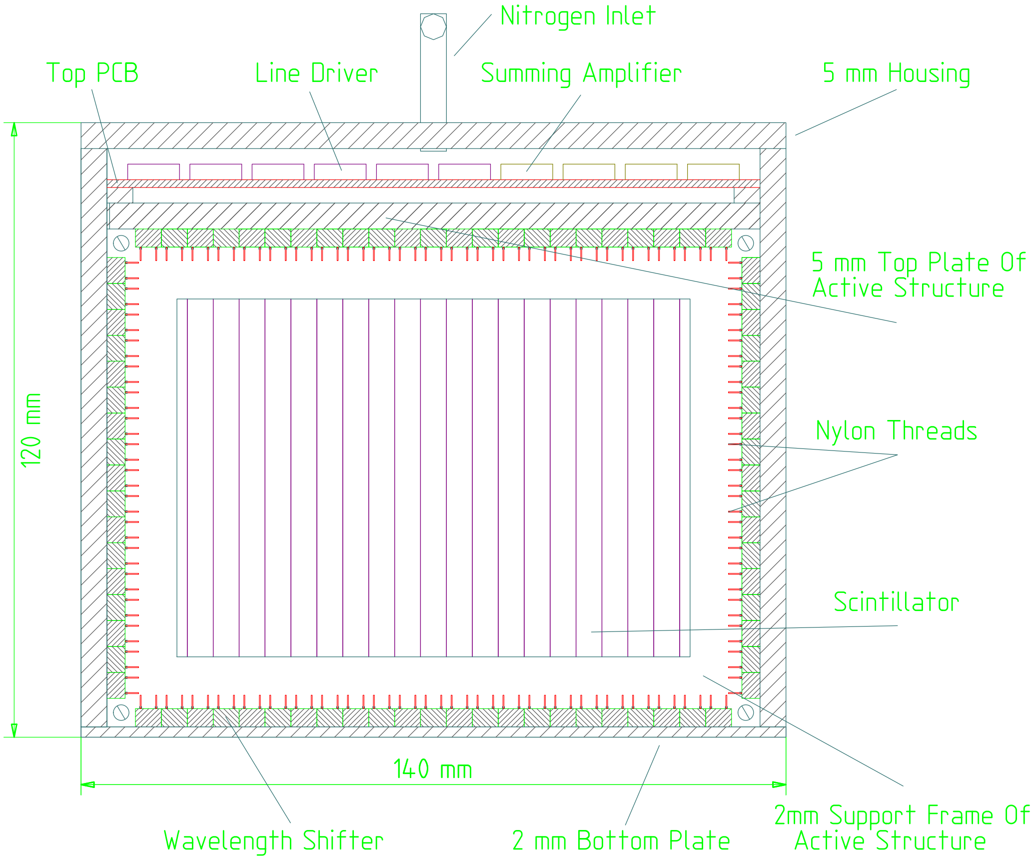

Figure 13: Front view of the mechanical structure; the front plate of the housing and the front PCB are removed.

3.2.3 Electronics Layout

Readout The readout of the wavelength shifters is done with photodiodes. They are arranged in arrays of two different length (18 and 24 photodiodes) as shown in figure 16. The specifications for the photodiodes are given in table 2.

The spectral response curve of the photodiodes [13] is shown in figure 17. We are currently considering the use of Si-PIN Diodes manufactured by Hamamatsu. The quantum efficiency is about 85 % even in the green wavelength region. This matches well the emission spectrum of the wavelength shifter F203 from Optectron which has its emission peak at 520 nm. As scintillator the S101 type from the same company may be used. These components are a likely choice for the EPC (see ref. [9] for more information).

The electronics readout of the photodiodes is done by charge sensitive preamplifiers, which are realized as ASIC's (Application Specific Integrated Circuits). Preamplifiers built with conventional discrete electronics would take more space than available. In addition the high power consumption would make cooling more difficult. A schematic overview of the ASIC is given in figure 18. There are 6 preamplifiers followed by shapers on one chip. With a shaping time of 200 ns the shaped signals are too slow for the trigger, making bunch crossing identification very difficult. Therefore the fast preamplifier signals

Parameter	Value
Length	15.0 cm
Width	14.0 cm
Height	12.0 cm
Weight(without housing)	12 kg
Weight(with housing)	≈20 kg
No. of W sheets	23
No. of sci sheets	24
No. of horizontal sci slabs per layer	18
No. of vertical sci slabs per layer	24
Total number of horizontal sci slabs	432
Total number of vertical sci slabs	552
Thickness of W sheets	2.5 mm
Thickness of sci sheets	3 mm
Density of W	19.3 g/cm^3
Density of sci	1.03 g/cm^3
Mean density (active structure)	8.55 g/cm^3
X_0(W)	0.35 cm
X_0(sci)	42.4 cm
Depth (X_0)	16.7
Molière Radius	1.25 cm
No. of photodiodes	168

Table 1: Calorimeter parameters for one subsystem

Parameter	Value
Diode Area	$3.5 \times 4.5\,\mathrm{mm}^2$
Capacitance	$10\,\mathrm{pF}$
Resposivity	0.35 A/W ($\lambda = 540\,\mathrm{nm}$)
Dark current	typ. $2\,\mathrm{nA}$
Homogeneity of array	$< 3\%$

Table 2: Specifications for a single element of the photodiode array

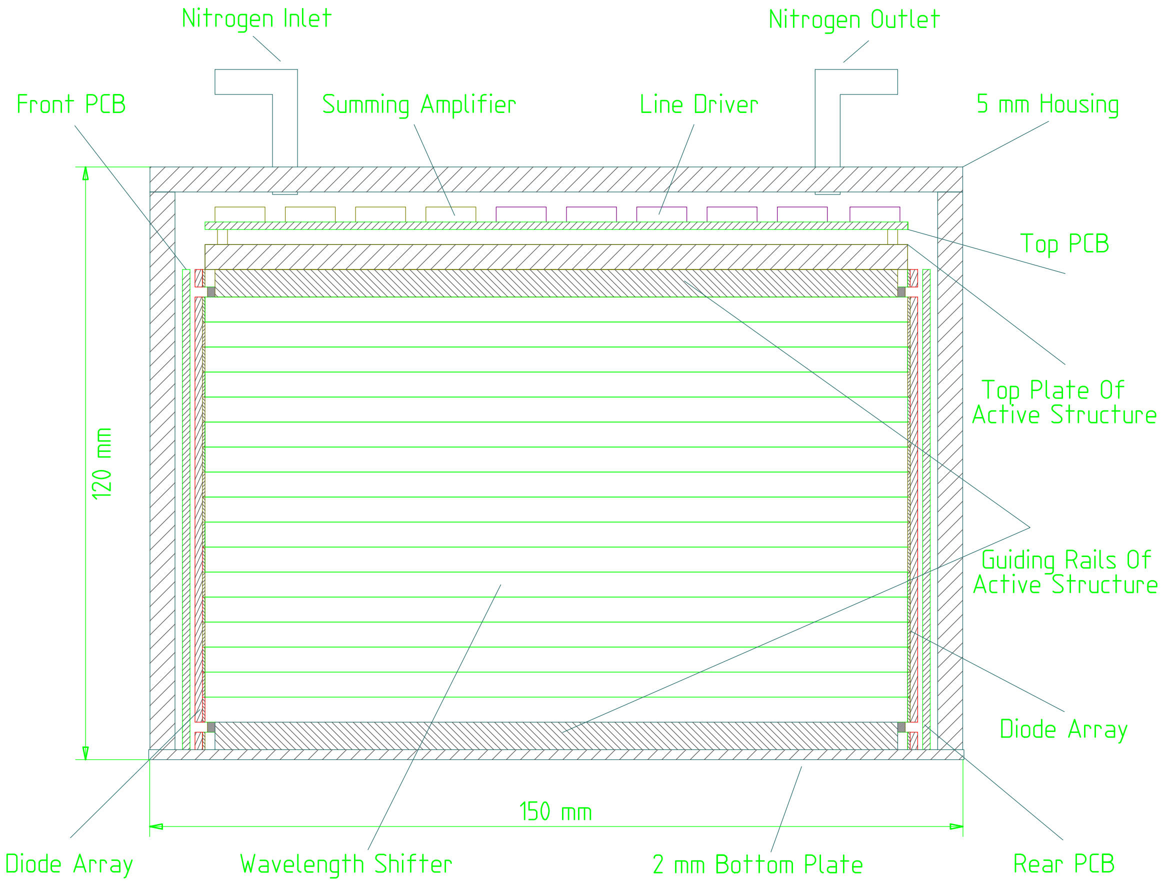

Figure 14: Side view of the EPC; the cover plate of the housing is removed.

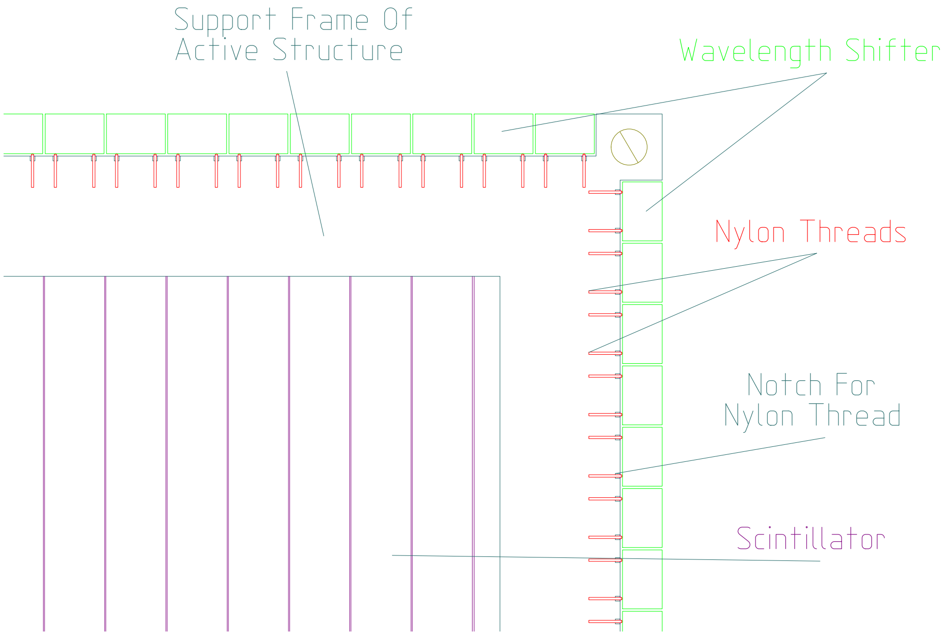

Figure 15: Magnified view of the front plate fixing the active structure and Nylon threads

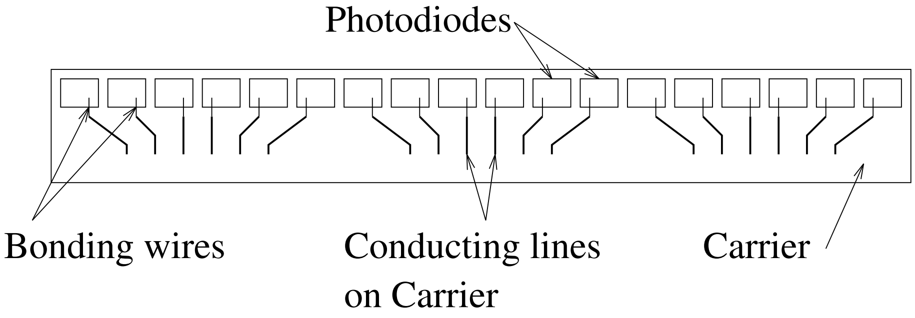

Figure 16: Array of photodiodes

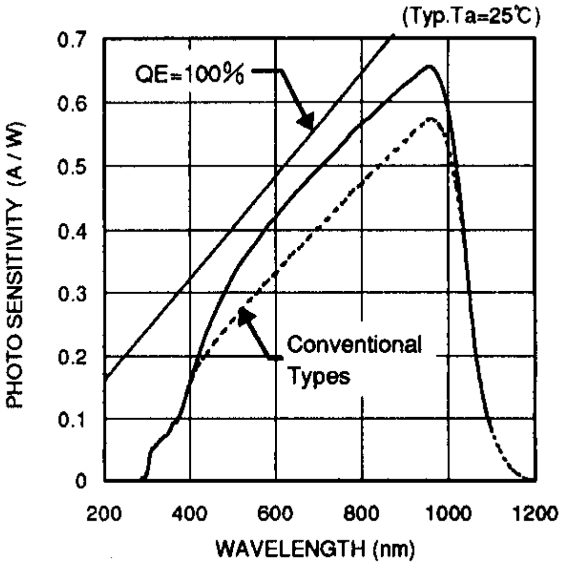

Figure 17: Spectral response of the photodiodes

(risetime ~30 ns) are summed on the chip to provide an input to the trigger signal. Simulated signal shapes of the preamplifier and shaper outputs can be seen in figure 19.

The noise performance of the calorimeter is determined by the noise of the preamplifiers alone. Therefore the minimization of the noise was a key task during the design process. The noise performance of the preamplifiers calculated analytically from the chosen design parameters is given by

$$ENC = 159\,e^- \; + \; 14.8\,\frac{e^-}{pF} \cdot C_l \; , \qquad (4)$$

where C_l is the load capacitance of the preamplifier and ENC means equivalent noise charge. For a load capacitance of 10 pF a rms ENC of 300 e^- is obtained.

A preamplifier was designed in the AMS (Austrian Micro Systems) 1.2 μm CMOS process. This amplifier was submitted for production at the beginning of February 1996 and is expected to be back at the beginning of April 1996. Experience obtained with a similar design in the Heidelberg ASIC laboratory has shown the validity of the above calculation [10].

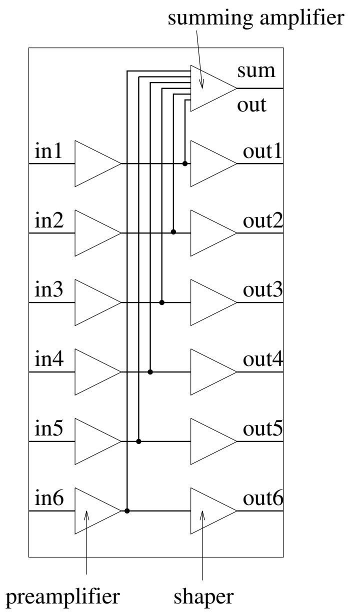

Figure 18: Schematical overview of the ASIC design

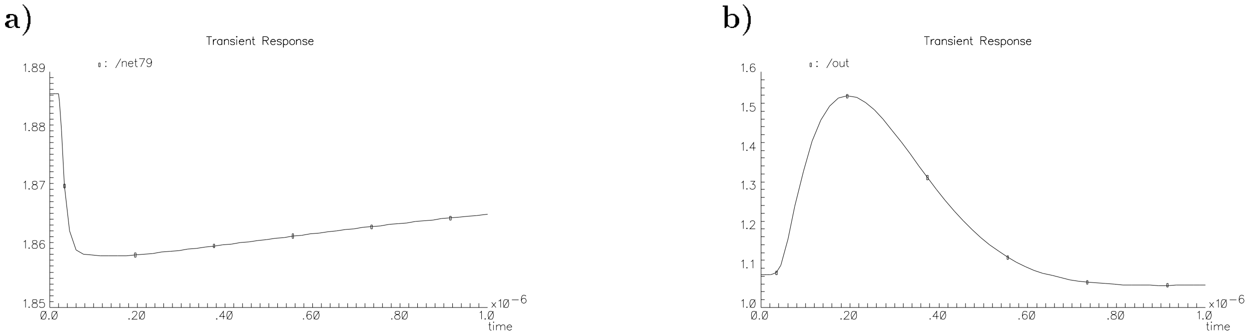

Figure 19: Signal shapes of **a)** preamplifier and **b)** shaper. Time is in seconds, vertical axis is in volts.

The preamplifiers are mounted on PCB's on the front and back plane of the active structure directly behind the photodiodes to avoid additional capacitive loading of the preamplifier inputs through connecting wires. On the front and rear PCB 14 ASIC's are mounted respectively. This amounts to $2 \cdot (2 \cdot 24 + 2 \cdot 18) = 168$ photodiodes to be read out for one calorimeter module, totaling 336 photodiodes for the complete calorimeter.

All single diode signals are brought to the top PCB where summing amplifiers and line drivers are located. A general scheme of the electronics on the detector is shown in figure 20. From each of the 14 ASIC's located on the rear and on the front PCB 7 signals are delivered to the top PCB. On the top PCB the signals from the front and rear diodes of one wavelength shifter are summed. This results in a reduction of readout channels by a factor two. The trigger signals are summed in such a way that four signals are provided. These correspond to the signals seen by all wavelength shifters located at the top, bottom, left and right sides respectively. A more detailed discussion of the trigger circuit is given in the next section. All signals are then transmitted by differential line drivers to the subsequent electronics. Differential transmission is chosen to avoid common

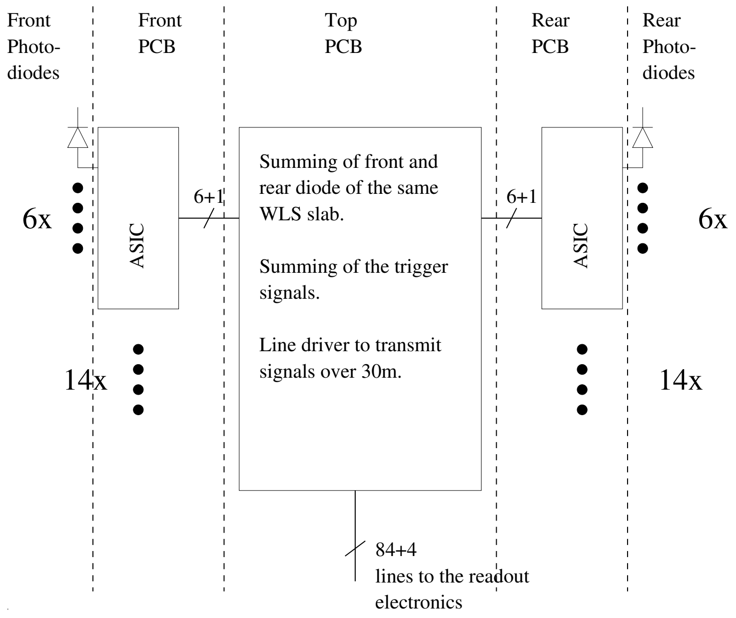

Figure 20: General scheme of the front end electronics for one calorimeter module

mode couplings from outside which would deteriorate the noise performance. The total number of readout channels amounts to 168 plus 8 signals for the trigger.

For further processing the readout electronics of the BEMC [11] can be used with a slight modification, namely to replace the BEMC shapers on the analog cards by receivers for the differential signals since the shaping is performed already on the chip.

Data Acquisition In total there are 168 readout channels and 8 channels for the trigger which we foresee to be read out by the standard H1 calorimeter readout [19]. The electronics previously used for the readout of the BEMC will be recovered for the readout of the EPC. This requires only slight modifications. The old H1 calorimeter event builder software for the BEMC readout can also be used for the EPC with minor modifications.

Trigger The trigger input signals are provided as analog sums of the signals of the four wavelength shifter rows for each calorimeter module. To generate a trigger signal it is required that all four trigger sums exceed a certain threshold at the same time. So called single-diode events are therefore efficiently suppressed because they would give rise to single large pulse heights in one row of wavelength shifters only.

It is planned to provide two levels of energy thresholds to form the final physics trigger of the VLQ. An OR of both calorimeter modules with high threshold will provide a scattered electron trigger. A lower threshold imposed on both modules will be used to record QED Compton events.

A disadvantage of the proposed trigger circuit is that there is no possibility to suppress the noise generated by the preamplifiers and channel-to-channel variations. The electronics noise contribution to the trigger smearing can be estimated to be $25\%/E[GeV]$. There are several reasons for channel-to-channel variations. First there are differences in the

Bit	Meaning	Threshold
HLUP	High trigger level of upper module (single electrons)	$\approx 8\,\mathrm{GeV}$
LLUP	Low trigger level of upper module (QED Compton)	$\approx 2\,\mathrm{GeV}$
HLLO	High trigger level of lower module (single electrons)	$\approx 8\,\mathrm{GeV}$
LLLO	Low trigger level of lower module (QED Compton)	$\approx 2\,\mathrm{GeV}$
SDUP	Single diode event in upper module	not yet known
SDLO	Single diode event in lower module	not yet known

Table 3: Trigger bits for the VLQ calorimeter

response of the photodiodes, specified to be smaller than 3%. Second there are channel-to-channel variations of the gain factors of the preamplifiers on one single chip of the order of 5%. The largest uncertainty in the homogeneity of channel response, however, are the chip-to-chip variations of the gain factor. They can amount to 30%. Thus for the trigger noise there are four contributions

$$\sigma_{Thr}/Thr = \sqrt{(3\%)^2 + (5\%)^2 + (30\%)^2 + (25\%/E[GeV])^2} \approx 30\,\% \; . \tag{5}$$

It is obvious that the main contribution to the threshold uncertainty are the chip-to-chip variations. There are several ways of overcoming this problem. One possibility is to select the chips by measuring the gain and rejecting chips with deviations greater than a certain tolerance. With this method the overall chip-to-chip variations can be reduced to about 10%. A second possibility is to transmit all the single trigger signals of the chips to the outside where an adjustment of the variations could be done. In total this would amount to 56 trigger signals to be transmitted to the electronics trailer. The third possibility is to foresee an adjustment mechanism on the detector itself. Due to severe space limitations and the use of higher trigger levels for threshold sharpening (L3, L4) the first method is currently favoured.

For the central trigger logic (CTL) 6 bits are foreseen, as listed in table 3. We prefer to form the final subtrigger at the CTL level instead of using look-up tables in order to use the monitoring possibilities for diagnostics.

3.2.4 Simulation Studies and Performance

Simulation Setup A detailed study of the calorimeter performance has been made using the program package GEANT [12]. The GEANT geometry is displayed in figure 21, using the geometrical layout and material composition as described in section 3.2.2 and summarized in table 1. The incident electron energy and direction have been varied. Each data point corresponds to 500 simulated events.

GEANT performs a complete treatment of shower development through active and passive materials and delivers energy deposition in the scintillator slabs and tungsten plates. This information can be converted into the parameters of interest, namely longitudinal and lateral shower containment, and energy and spatial resolution as a function of energy and impact point.

Energy Resolution and Shower Containment of the EPC

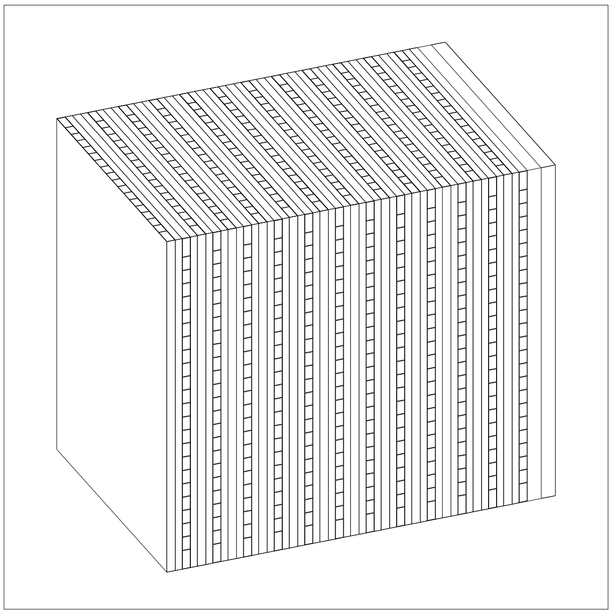

Figure 21: Geometry of the calorimeter in the GEANT simulation. The front plate of the housing and the air gap for the electronics are included.

Resolution Performance The energy distribution in the scintillator for 30 GeV incident electrons is shown in figure 22. The distribution is Gaussian, a fit gives an energy resolution of $\sigma_E/E = 3.5\,\%$ at $E = 30$ GeV. In the following all values for means and resolutions are obtained from Gaussian fits to the data.

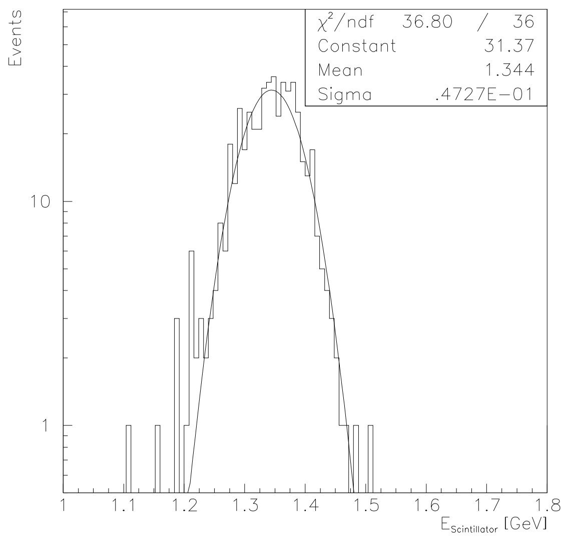

Figure 22: Energy distribution in scintillator for electrons of 30 GeV impact energy. The curve represents a Gaussian fit to the data.

The response of the calorimeter as a function of the electron energy is displayed in figure 23. The calorimeter exhibits excellent linearity for energies between 5 GeV and

30 GeV. The deviations are smaller than one percent.

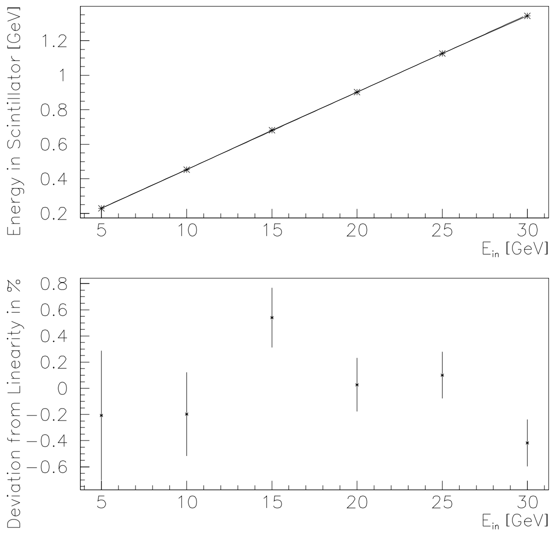

Figure 23: Linearity of the EPC response. The upper figure shows the energy deposit in the scintillator versus the incident energy. The lower plot shows the deviation from a linear fit to the simulated points.

One of the most important characteristics of a calorimeter is its energy resolution. The energy resolution versus the impact energy is shown in figure 24. The energy dependence of the resolution can be parametrized by

$$\frac{\sigma_E}{E} = \sqrt{\left(\frac{P_1}{\sqrt{E[GeV]}}\right)^2 + (P_2)^2}\ . \tag{6}$$

A fit results in values of $P_1 = (14.3 \pm 0.6)$ % for the sampling term and $P_2 = (2.1 \pm 0.2)$ % for the constant term (see curve in figure 24).

In order to estimate the electronics noise contribution, the BEMC [11] has been used as a reference. This is a good approximation since its structure is very similar to that of the EPC. In the BEMC a 1 GeV electron liberates a charge of 17040 electrons in the photodiodes. Assuming for both calorimeters the same conversion efficiency from energy absorbed in the scintillator to charge on the photodiode, the photodiode charge seen by the EPC can be calculated

$$\begin{aligned} Q_{EPC} &= Q_{BEMC} \cdot \frac{E^{Sci}_{EPC}}{E^{Sci}_{BEMC}} \\ &= 17040\,[e^-] \cdot \frac{45.9\,\text{MeV}}{104.7\,\text{MeV}} \\ &= 7470\,[e^-]\ . \end{aligned}$$

Here E^{Sci}_{EPC} and E^{Sci}_{BEMC} are the energy deposits in the EPC and the BEMC scintillators, respectively. Since the EPC is read out at both ends, one expects a charge of $14940\,e^-$ in the photodiodes caused by a 1 GeV electron. In the final energy determination, several

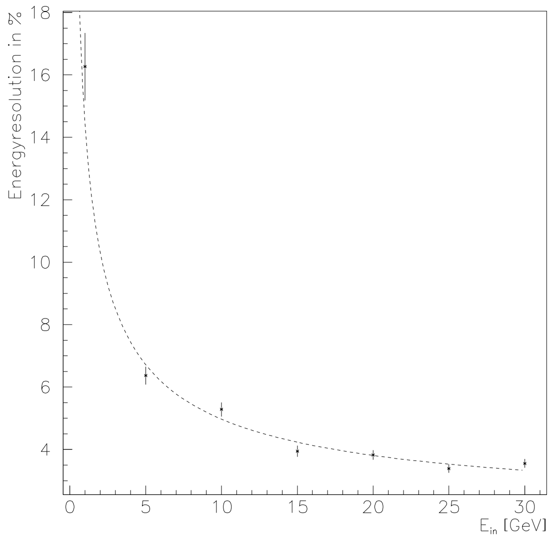

Figure 24: Energy resolution versus the incident electron energy. The curve represents a fit to the parametrized energy resolution containing a sampling and a constant term.

channels will be summed, thereby increasing the noise contribution. Suppose that two horizontal and two vertical scintillator slabs are summed to obtain the energy. From the simulation it is known that these four slabs contain 75% of the shower energy. Thus the response to a 1 GeV electron will be a charge of $0.75 \cdot 14940\, e^- = 11205\, e^-$. Each slab is read out by 4 photodiodes, thus the total noise is $\sqrt{4 \cdot N_{vert} + 4 \cdot N_{hor}}\, ENC = \sqrt{16} \cdot 300\, e^- = 1200\, e^-$ with ENC, the rms noise of one preamplifier, taken from eq. 4. The noise contribution per GeV then becomes $1\,\mathrm{GeV} \cdot (1200\,\mathrm{e}^-/11205\,\mathrm{e}^-) = 0.107\,\mathrm{GeV}$. The final energy resolution for the EPC can now be written as

$$\frac{\sigma_E}{E} = \sqrt{\left(\frac{14.3\%}{\sqrt{E[\mathrm{GeV}]}}\right)^2 + (2.1\%)^2 + \left(\frac{0.107\,\mathrm{GeV}}{E[\mathrm{GeV}]}\right)^2}\,. \tag{7}$$

Due to the good understanding of the BEMC (data and simulation) we are confident that the simulation and noise estimate for the EPC are reliable.

Shower Containment Average longitudinal and lateral shower profiles of 30 GeV electrons are shown in figure 25. It is clearly seen that the shower is not fully contained in the longitudinal direction, which contributes to the constant term in the energy resolution. Since the available space for the VLQ is limited, the calorimeter cannot be made longer without worsening the overall VLQ performance. However, the expected calorimeter performance is sufficient for the physics to be done. In the lateral direction the containment is very good for central impact. The shaded area in figure 25 b) contains 95 % of the shower energy. The Molière radius is calculated to be 1.25 cm.

The lateral shower containment becomes worse near the edge of the calorimeter. To investigate this effect a 30 GeV electron beam at normal incidence was scanned over the calorimeter area, starting from the center along the y (vertical) direction. The energy resolution and response as a function of the y coordinate are shown in figure 26. As

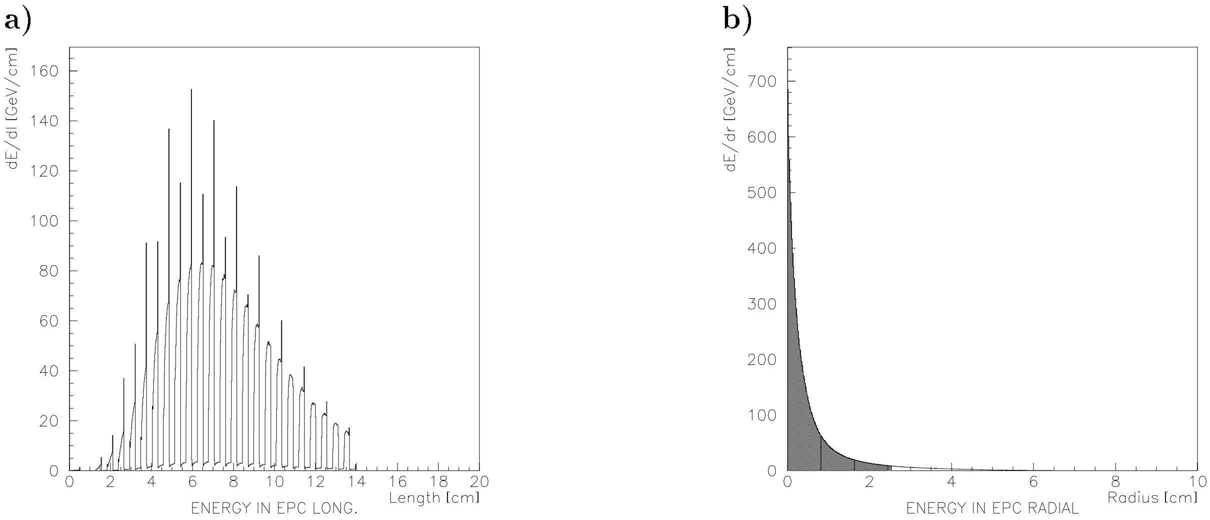

Figure 25: **a)** Longitudinal and **b)** lateral shower profiles of 30 GeV electrons

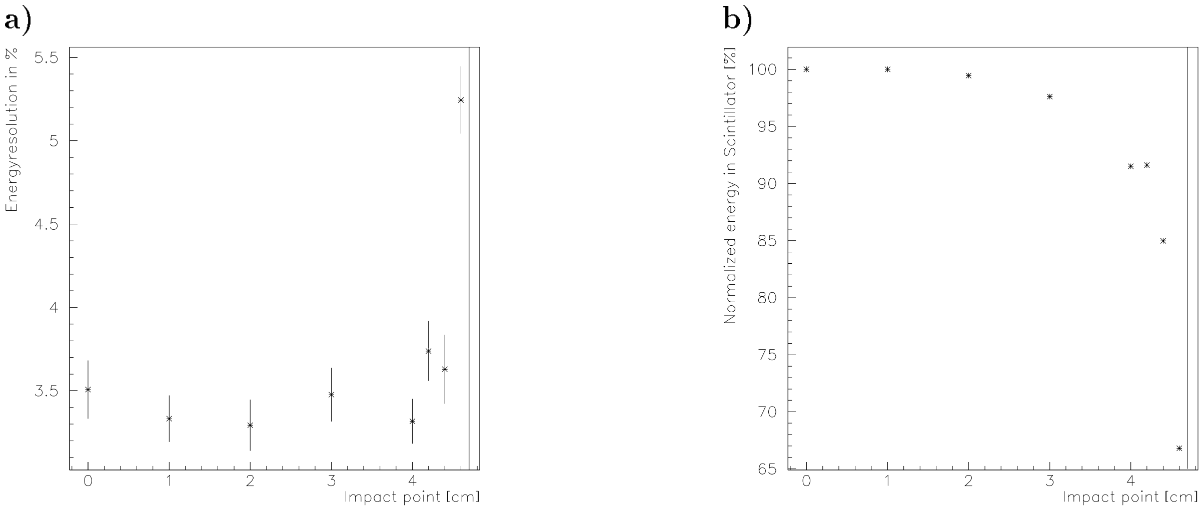

Figure 26: **a)** Energy resolution and **b)** energy containment versus impact point. The horizontal line at 4.9 cm represents the calorimeter edge.

expected the relative energy absorbed in the scintillator, shown in figure 26 b), is reduced towards the edge of the calorimeter and therefore has to be corrected. For this correction the impact point has to be known precisely, which can be achieved with an accuracy of $\sim$ 1 mm for electrons above 5 GeV. The energy resolution (figure 26 a)) does not deteriorate until the beam reaches a distance of 3 mm from the calorimeter edge. At a distance of 1 mm from the calorimeter edge the resolution is still of the order of 5%. This feature of the EPC, together with its good spatial resolution, makes it possible to almost fully use the geometrical acceptance of the EPC.

Spatial Resolution The spatial reconstruction of the EPC is obtained using the four-fold projective readout of the scintillator slabs. The coordinates are calculated from the center of gravity. In the simulation electronic noise has been added and its effect on the spatial reconstruction has been studied varying the noise cuts (typically 1 or 2 σ). To extract the spatial resolution from the simulation data, the distance between the actual and the reconstructed impact point has been calculated. A fit to the distribution was made using the function

$$P(x) = P_1 \cdot x \cdot \exp\left(\frac{-x^2}{2\,\sigma_x^2}\right) , \tag{8}$$

where σ_x is the spatial resolution. Results for 5 GeV electrons are shown in figure 27.

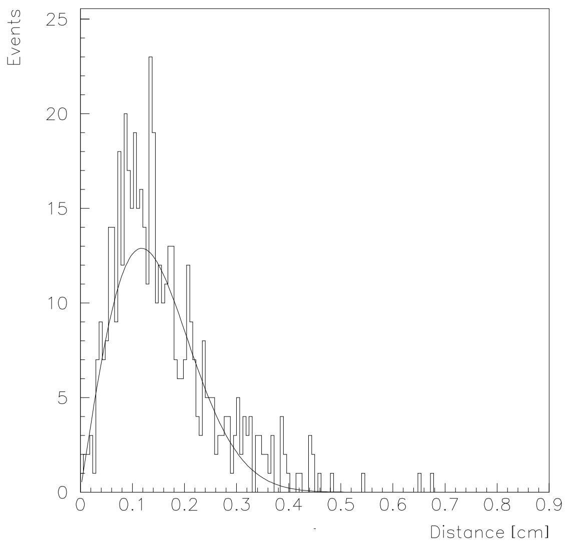

Figure 27: Distance distribution between actual and reconstructed impact point for 5 GeV electrons with a noise cut of 2σ. The curve is the result of a fit to eq. (8) with a spatial resolution of $\sigma_x = 1.1\,\mathrm{mm}$

The spatial resolution as a function of the impact energy is plotted in figure 28. The results were obtained with a noise cut of 2σ. The spatial resolution is in the order of 1 mm and better for energies larger than 5 GeV. These results were obtained with electrons hitting the calorimeter in the central region. The spatial resolution will deteriorate when approaching the calorimeter edge.

Figure 29 shows the variation of position resolution for different widths of the scintillator slabs. It turns out that the choice of 5 mm scintillator width gives a good spatial resolution. Further reduction of the width would improve the resolution only marginally, but would increase the number of readout channels.

3.3 The Tracking System

The tracking system of each of the two spectrometer arms consists of two double layers of semiconductor detectors separated by 13 cm along the beam direction. A perspective view is shown in figure 30. The two planes of each double layer measuring the X (layers $V1$, $V2$) and Y (layers $H1$, $H2$) positions by vertically and horizontally oriented strips, have an active area of $\sim 8{\times}10\ \mathrm{cm}^2$. The detector material will be semi-insulating Gallium Arsenide (SI-GaAs) with the design and production being done at the I. Physikalisches Institut in Aachen [14] with support from ISI-KFA, Forschungszentrum Jülich. The motivation to use GaAs as detector substrate is threefold:

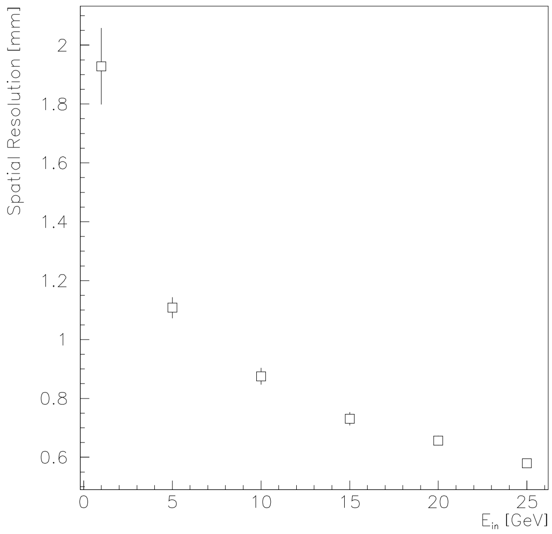

Figure 28: Spatial resolution versus electron energy

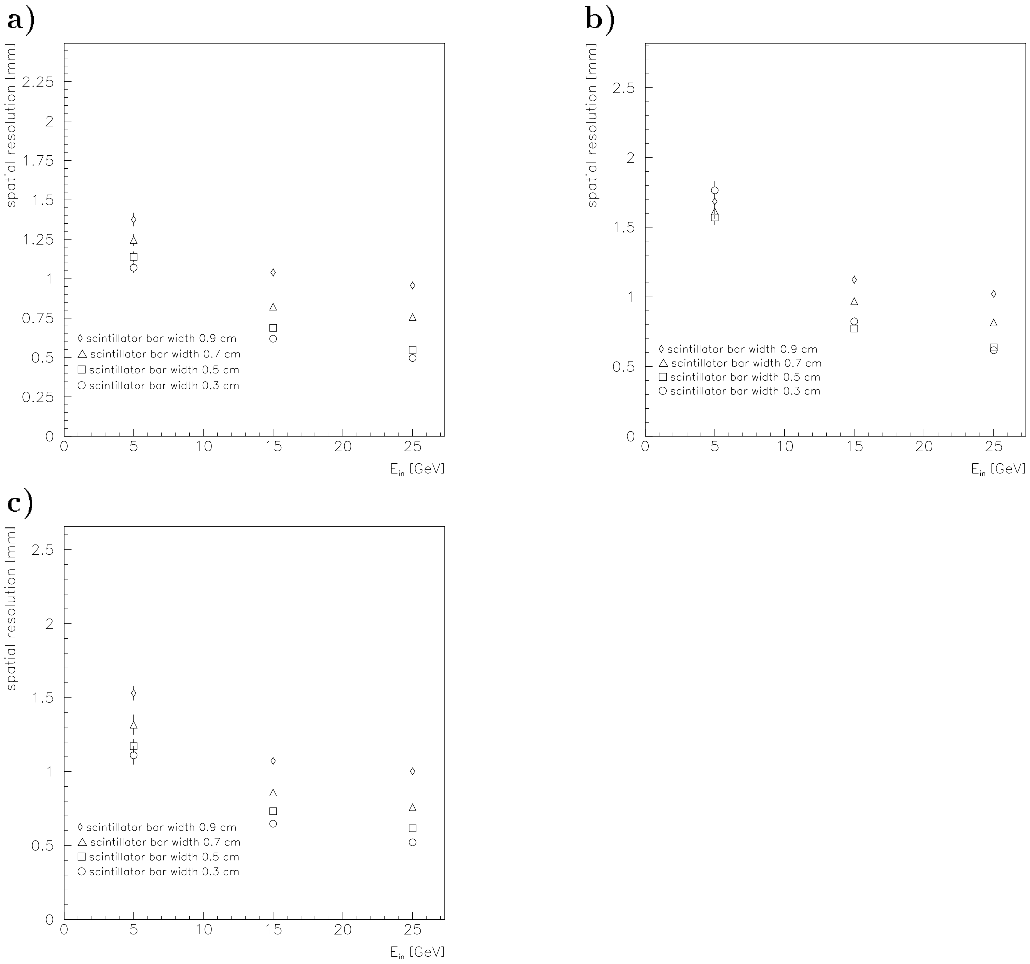

Figure 29: Spatial resolution versus energy for different scintillator widths and noise conditions. **a)** without noise; **b)** with noise, noise cut $1\,\sigma$; **c)** with noise, noise cut $2\,\sigma$.

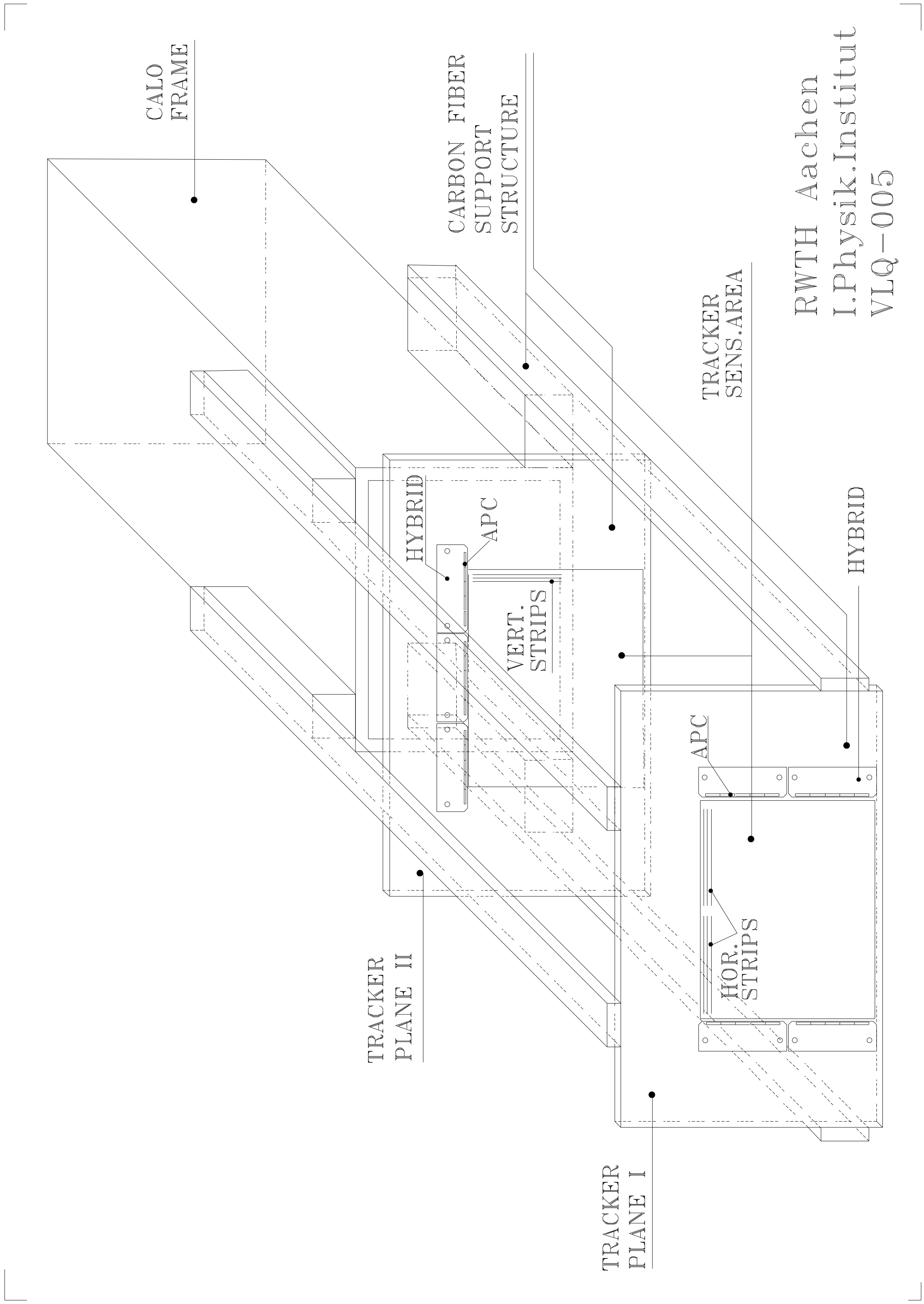

Figure 30: Perspective view of the upper VLQ subsystem showing the calorimeter and the tracker with its support structure

- expertise and facilities in our institute concerning processing, handling, assembling and testing these detectors
- lower cost in comparison with silicon when working silicon detectors are bought from commercial suppliers
- we have measured that GaAs detectors can stand γ ray doses (from a ^{60}Co radioactive source) up to 100 Mrad without any deterioration of the performance [16]. As a consequence we do not expect any damage due to synchrotron radiation.

The basic detector units are cut from 4"–wafers with a thickness of 250 μm which are provided by a commercial supplier [15]. The readout pitch equals the strip pitch of 62.5 μm with an aspect ratio (ratio of strip width to strip pitch) of 0.5. Strips and backplane are processed as Ti-Pt/Au Schottky contacts. Guard-rings, integration of coupling capacitances and passivation are applied in the usual way as for silicon detectors. The detectors are biased by punch-through from a biasing pad separated by 5 μm from the strips. A plane view of a basic unit is shown in figure 31 and a cross-sectional view is given in figure 32.

For the (ac-coupled) readout and the data acquisition we rely on the system which is used for the silicon trackers of the BST and CST detectors of H1 [17], i.e. the APC chips for the front end mounted on the appropriate hybrid boards and the OnSiRoc controllers for the readout. This readout chain has to be optimized and adapted to the GaAs detectors. The support of the the readout units containing detectors and hybrid boards is made of a low mass high thermal conductivity carbon fiber composite (which also can act as a heat bridge for the power dissipated by the electronics, see figure 30).

The two basic detector units for the layers $H1$ and $H2$ are read out on both the left and the right side, the strips not being connected together in the middle. The strips are bonded, via pitch adapters, to the APC's on the hybrid boards (2 hybrid boards on either side serving 5 APC's each) which are glued to the above mentioned carbon fiber board. The hybrids are connected to the so-called repeater board by a multi-line polyimid flexible cable. The repeater board receives the control signals from the OnSiRoc and distributes them to the hybrids, it receives the strip signals which are read out serially and amplifies them for transmission over $\sim 50m$ of a bipolar line. Furthermore it contains passive filter elements for the different voltage supplies. The repeater boards are fixed to the housing of the calorimeter. A carefull em shielding protects the frontend electronics against external noise sources and prevents emission of internal signals to the rest of the detector. The OnSiRoc and the DAQ is situated in a crate in the Si-tracker area (trailer-lower level).

The readout for the basic detector units for the layers $V1$ and $V2$ is done in a similar way. The strips are read out only on one side: at the top (for the upper part of the VLQ) and at the bottom (for the lower part of the VLQ), requiring per layer 3 hybrids (one with 5 APC's and two with 4 APC's). The connections to the repeater boards are done in the same way as for the layers $H1$ and $H2$.

The serial readout of the APC's will be performed by a special FADC mezzanine board together with a commercially available CPU on a VME board (the latter is the RIO unit of the CES company with a power-PC as CPU). One processor serves 8 channels. There will be two processors for the VLQ, one for the upper part and one for the lower part. Each of the modules H1, H2, V1 and V2 is read out by 2 channels. The readout

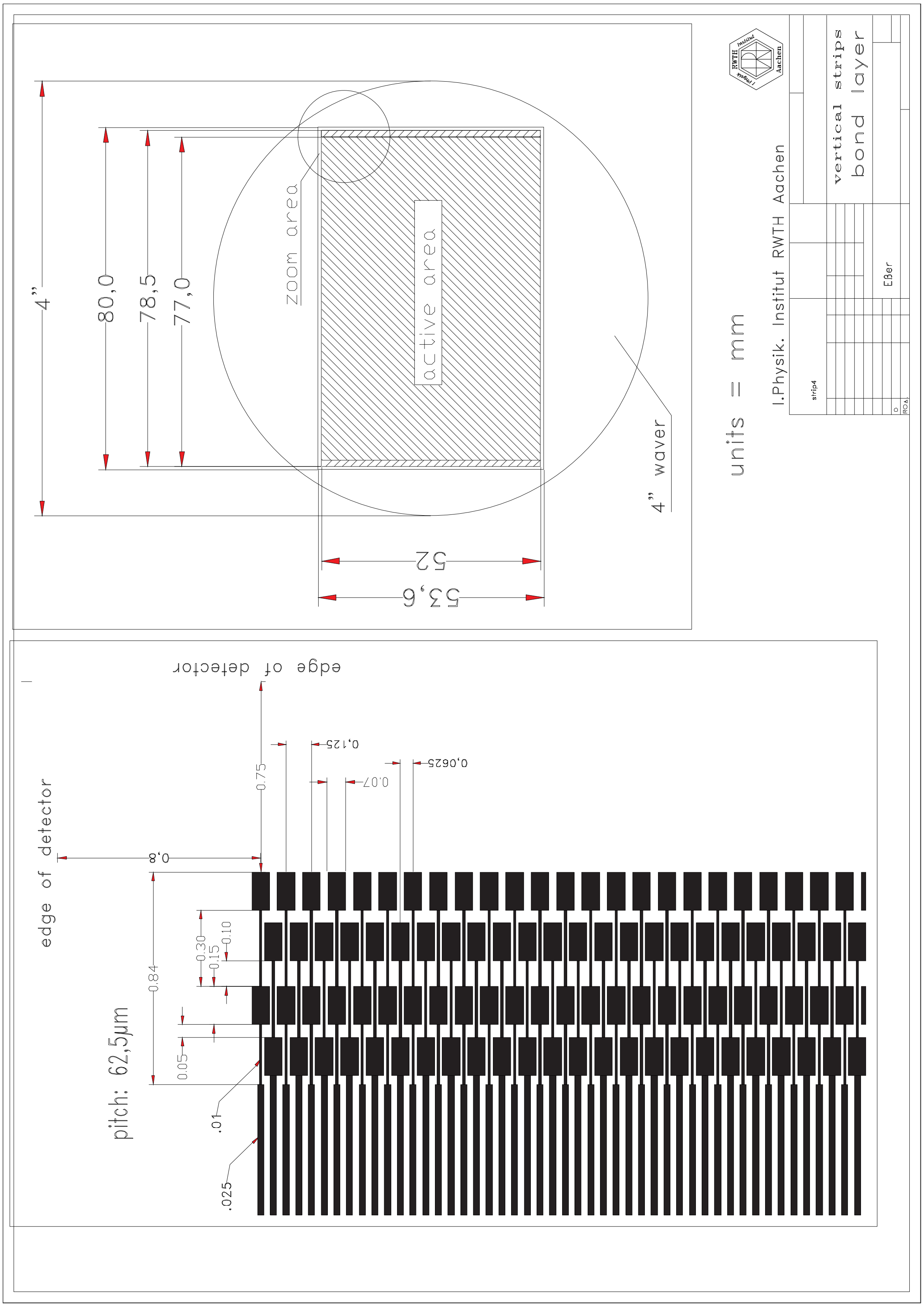

Figure 31: Plane view of the basic detector unit on the 4”-wafer and a detailed view of the bond-pad structure frequency will be $\sim$ 2 MHz so that up to 1280 strips (10 APC's) are read out within 640 μs, well before the arrival of the L3 keep signal (800 μs). After the data are read to the raw data buffers of the RIO boards, the pipeline of the APC is restarted and any further processing is asynchronous with respect to the front end data taking. The memories allow for multievent buffering. The readout scheme and data flow are sketched in figure 33.

We think that this system can be easily incorporated into the DAQ branch of the BST/CST.

Based on our experience with a similar SI-GaAs detector [18] we expect a mean signal of $\sim$ 20000 electron/hole pairs for a minimum ionizing particle traversing the detector, which leads to a signal to noise ratio for the vertical (horizontal) strips of $S/N \sim 15$ ($\sim$ 20) for the expected noise of the APC-preamplifier: $\sim$ 1250 ($\sim$ 1000) electrons for the strip capacitance of $\sim$ 15 pF ($\sim$ 10 pF). The spatial resolution per plane, based on the digital information only, amounts to $\sim$ 18 μm (= pitch/$\sqrt{12}$). However, applying center of gravity methods (linear algorithm or so-called η-algorithm) using the analog signal information will allow an improvement of the resolution to $\sim$ 10 μm.

The parameters of the tracking system are summarized in table 4.

Parameter	Value
Detector thickness	250 μm
Strip pitch	62.5 μm
Readout pitch	62.5 μm
Aspect ratio	0.5
Length of horizontal strips	2×50 mm
Length of vertical strips	80 mm
# of 4”–wafers	16
# of detectors (80.0×52.8 mm^2)	16
# of horizontal strips	10240
# of vertical strips	6656
# of readout channels	16896
# of APC's	132
# of hybrid boards	28
# of OnSiRoc	2

Table 4: Parameters of the tracking system

3.4 The Time–of–Flight System

The trigger signal based on the energy deposition in the VLQ calorimeter can safely determine the bunch crossing of the event origin (t_0), but is not able to distinguish between proton induced background (beam-wall or beam-gas) and the secondaries from ep collisions originating at the interaction point. We therefore intend to incorporate a time-of-flight (TOF) system into the proposed VLQ setup in very much the same way as it was used for the BEMC until 1994. We thereby maintain the possibility to use a “stand-alone” calorimetric trigger based on the energy depositions in the calorimeter only, especially for QED Compton events with minimum or no hadronic activity. Beside the main goal to

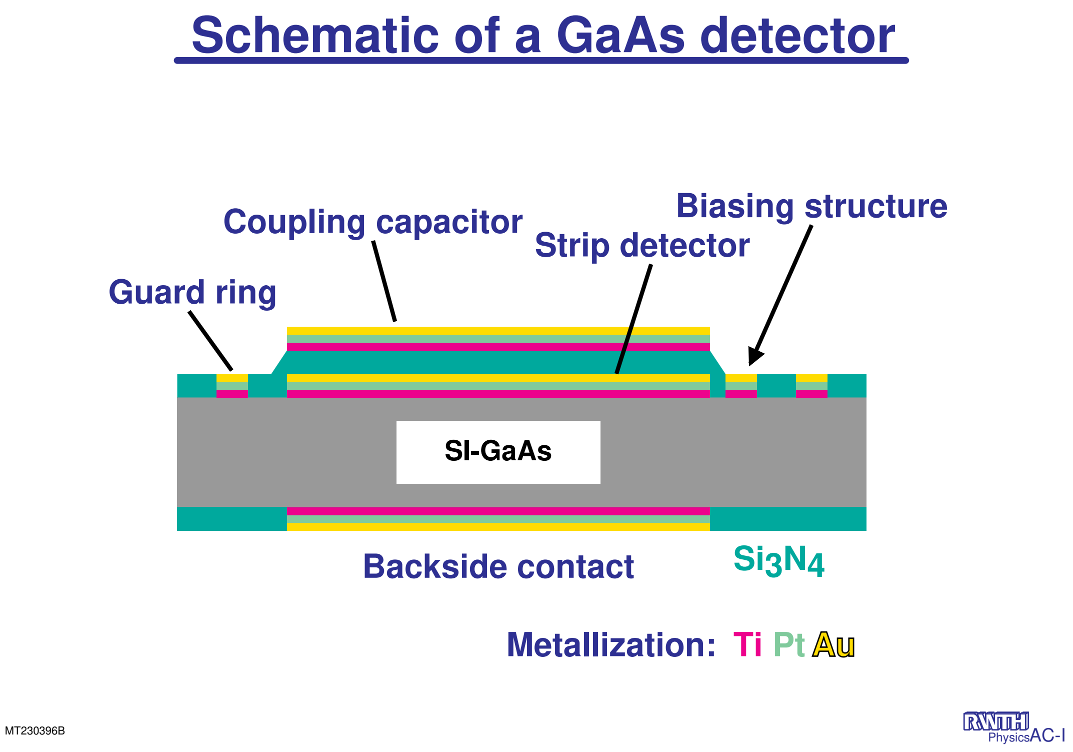

Figure 32: Cross section of the processed wafer

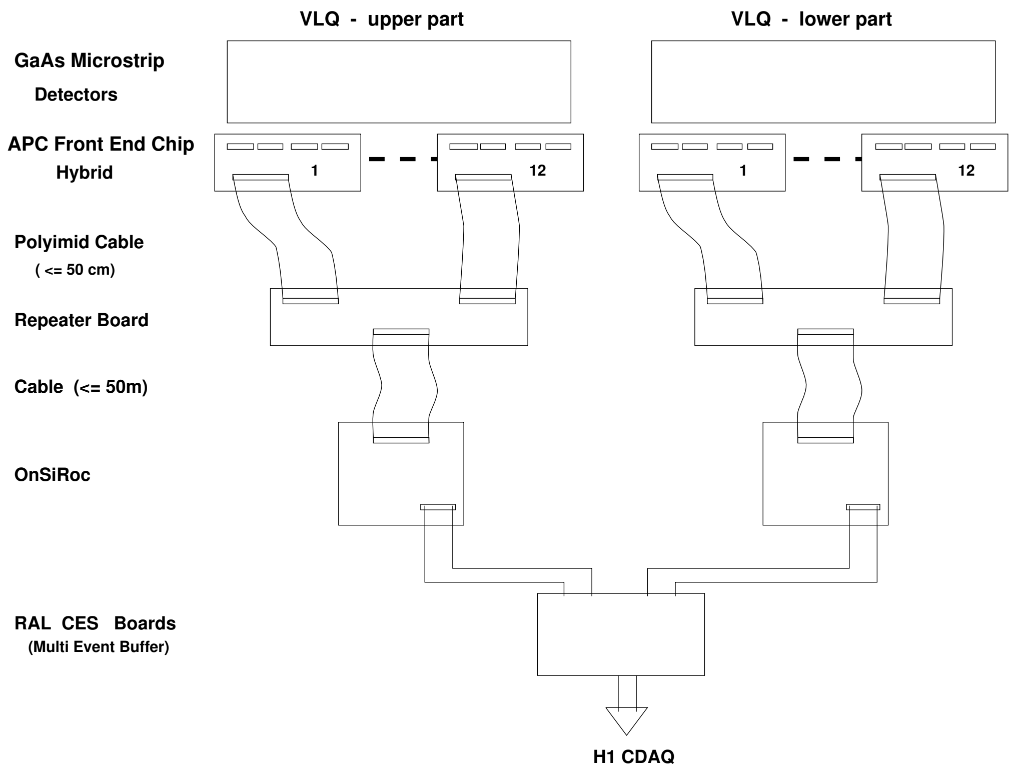

Figure 33: Sketch of the readout and data flow of the VLQ tracking system

veto calorimetric triggers originating from proton induced background, the TOF system will provide vital information indicating whether background conditions are acceptable for moving the VLQ into its measuring position.

We foresee to install two circular scintillator planes directly behind the calorimeter. They consist of two half-shelves each, with an outer radius of 200 mm, read out by a 1 inch photomultiplier of the type Hamamatsu R5500, as operating in the SpaCal.

The hole for the beampipe will be adapted to its hexagonal shape to the closest distance; this guarantees complete geometrical coverage of the calorimeter including the wave length shifters. The scintillator plates and all necessary mechanical parts will be machined in the University of Prague.

The thickness of the scintillator plates will be optimized to collect enough light in the photomultipliers, and to minimize the necessary space in z direction. Acceptable values at this stage of the technical design are 5 mm for the scintillator planes and 3 mm for a lead foil in between, in order to suppress random coincidences due to synchrotron radiation. This results in less than 15 mm space along the z direction. The total weight of such a structure, including photomultipliers and part of the cables, will not exceed 4 kg and can be supported directly by the beam pipe. Depending on the final scintillator plate thickness we foresee a supporting structure mounted to the compensator flange. The photomultipliers will be glued directly to the outer edges of the scintillators.

The complete NIM based electronics and the high voltage power supply, together with the slow control system of the four photomultiplier channels of the backward TOF [19] used during the 1995 luminosity period, will be used.

No radiation damage to the scintillator material of the backward TOF with an inner radius of 7 cm was observed during the 1995 luminosity period. Due to the closer distance to the beam larger radiation doses for the innermost part of the scintillator planes are expected. The radiation facility in Prague will be used to study the radiation damage to different scintillator types. In addition, spare sets of scintillators will be produced to allow a complete replacement if necessary.

In order to understand the behaviour of photomultipliers in the inhomogeneous magnetic field close to the compensator, H1 is installing a TOF system at the position foreseen for the VLQ TOF, with 20 mm thick scintillator plates and inner and outer radii of 67 mm and 250 mm, respectively, already for the 1996 running period. The experience gained during the first months of 1996 HERA running will be used for the final VLQ TOF system design.

4 Synchrotron Radiation Background

In order to provide zero crossing angle electron-proton collisions it is necessary to steer and focus the electron beam quite close to the interaction regions, resulting in the emission of large amounts of synchrotron radiation, primarily in a “fan” in the machine plane and directed out of the ring. All sensitive detectors must be shielded from this radiation. To this end the beam-line close to H1 contains a series of collimators and absorbers, the aim being to ensure that neither direct nor once reflected synchrotron radiation can enter the sensitive regions of the detector. These collimators and absorbers are:

1. Collimator C3 at $z = 5.6\,\mathrm{m}$ with inner radius 12 mm, thickness 12 cm and made of tungsten. This collimator absorbs a large amount of the direct synchrotron radiation emitted by the electron beam. The edge that is struck becomes a source of secondary "edge scattered" synchrotron radiation photons. Though this is not at the moment the case, it is assumed here that this edge has been machined so the surface is at an angle to the z axis in the machine plane corresponding to the mean angle of incidence of the direct synchrotron radiation that falls on it. This angle is about 4 mrad. This reduces the amount of edge scattering by a factor of about twenty.

2. Collimator C4, at $z = 2.15\,\mathrm{m}$, made of tungsten, and with adjustable inner radius. This collimator absorbs a large part of the secondary radiation emitted from the edge of C3. The studies here were performed with the inner radius set to 17 mm which provides adequate protection for the central jet chamber (CJC) and central and backward silicon detectors (CST and BST respectively) without moving C4 into the primary synchrotron radiation fan.

3. Collimator C6, at $z = -3.21\,\mathrm{m}$, made of tungsten.

4. Absorber A24, at $z = -24\,\mathrm{m}$, made of tungsten with a special silver and copper low albedo coating. This absorbs a large amount of direct synchrotron radiation that has passed through the entire detector close to the electron beam and in the plane of the electron ring. It is, via "back scattering", the second important source of secondary synchrotron radiation. Collimator C6 is designed to prevent this back scattered radiation from reaching the sensitive parts of H1.

The problems associated with synchrotron radiation that may arise as a result of the installation of the modified beam pipe and the VLQ are the following:

1. The beampipe may be struck by primary synchrotron radiation causing it to become a source of secondary radiation and hence prevent operation of sensitive elements of the H1 detector.

2. The number of synchrotron radiation photons hitting the VLQ tracker may cause so many spurious signals that its performance, particularly with regard to pattern recognition, is significantly degraded.

3. The radiation dose the VLQ receives may be so large that it ceases to function.

These problems are addressed in the following. The beampipe considered was as proposed above. The effects on the sensitive detector components, the central and backward silicon trackers (CST and BST respectively), the central inner proportional chambers (CIP), the central inner z chambers (CIZ) and the CJC were considered.

The study was performed by using Monte Carlo methods to simulate:

1. The primary synchrotron radiation emitted by the electron beam in the region from 24 m to 5.5 m before the H1 interaction region, using the standard beam optics.

2. The mechanisms whereby C3 and A24 emit secondary synchrotron radiation, Compton scattering, Rayleigh scattering and fluorescence all being considered.

3. The interactions of secondary photons in the H1 detector, the energy lost in the active and passive components of the detector being considered.

The study was done for the most difficult environment that H1 and the VLQ is likely to face, namely an electron beam of energy 30 GeV and current 60 mA.

Results Figure 34 shows the number of primary synchrotron radiation photons with energy greater than 5 keV as a function of x and y at the position of the VLQ. The rate is $3.1 \times 10^{17} \gamma\,\mathrm{s}^{-1}$ which corresponds to a power of 1.4 kW. The minimum lateral radius of the beam pipe at this position is 4.9 cm, the minimum vertical radius 2.0 cm and hence the beam pipe is not in danger of being hit by direct synchrotron radiation.

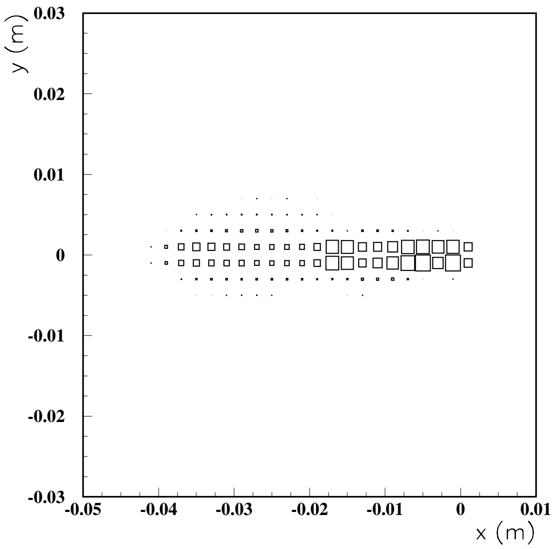

Figure 34: Rate of primary synchrotron radiation photons with energy above 5 keV at the position of the VLQ, x increases towards the outside of the ring

Another potential problem occurs at $z = -2.2\,\mathrm{m}$, where the radius of the beam pipe changes from 4.5 cm to 5.5 cm. The synchrotron radiation profile at this point is shown in figure 35. Also here the beam pipe is not hit by direct synchrotron radiation. This is, however, the point at which the beam pipe is closest to the synchrotron radiation fan and the margin for error here is small. The beam pipe installation must be precise and the effect of any changes in the electron beam steering on the direct synchrotron radiation fan at this point carefully considered.

Although no direct synchrotron radiation enters the VLQ, it is hit by secondary radiation from both C3 and A24. The radiation from A24 is easily shielded, for example by a collimator such as the existing C6. The radiation from C3 poses a more serious problem. Monte Carlo simulation shows that the number of hits from this source registered in the GaAs of the first VLQ tracking layer for the above beam conditions is about 10 per bunch crossing, assuming that a photon must deposit an energy of 40 keV in the GaAs before a hit is registered. The distribution of these hits as a function of x and y is shown in figure 36. They are seen to be concentrated at the inner edge of the VLQ tracker. The results for the second tracking plane are similar.

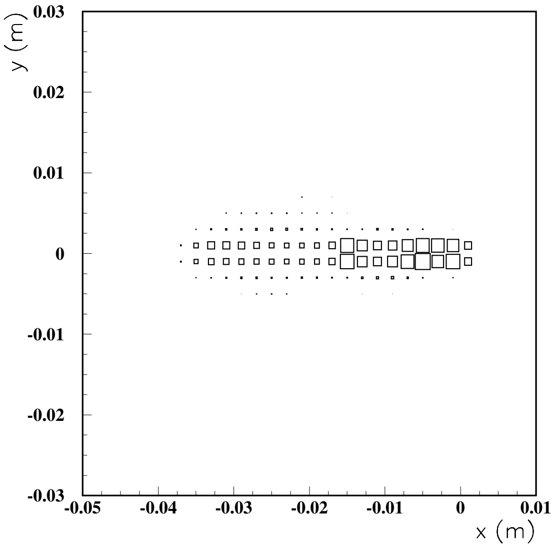

Figure 35: Rate of primary synchrotron radiation photons with energy above 5 keV at $z = -2.2\,\mathrm{m}$

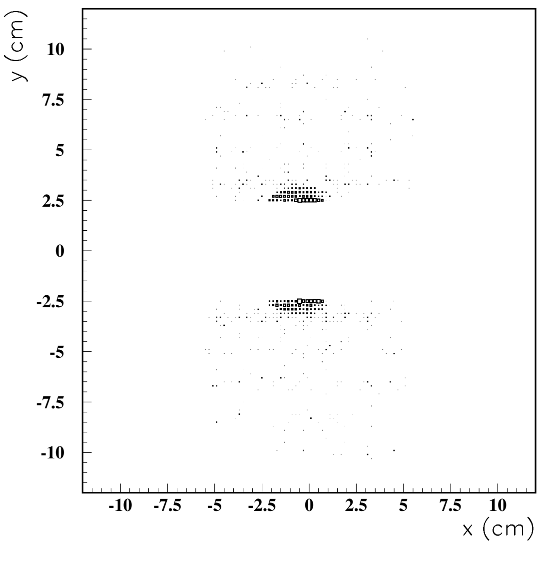

Figure 36: Distribution of hits due to synchrotron radiation in the first VLQ tracker layer

The hit rate on the VLQ tracker would be higher were it not for the stainless steel section of beampipe covering the innermost part of the VLQ. This provides an effective depth of 4.9 mm of shielding, absorbing photons that would otherwise enter the VLQ. The absorbed power is expected to be about 50 mW and it must be ensured that this does not lead to overheating of this section of beampipe.

The dose absorbed by the VLQ tracker in a nominal year of 10^7 s of running is found to be about 100 krad and hence will not suffer excessive radiation damage due to synchrotron radiation.

Conclusions The beam pipe proposed in conjunction with the VLQ will not be struck by primary synchrotron radiation if the electron beam steering remains as it is. The margin for error is small however, particularly at $z = -2.2$ m. The number of spurious hits that is to be expected in each layer of the VLQ tracker as a result of synchrotron radiation is of the order of 10 per beam crossing. These conclusions depend on the successful modification of C3. If the modification is not performed, the above numbers must be multiplied by a factor of about twenty.

Since the synchrotron radiation background is most severe at the inner side of the VLQ, it is always possible to retract the detector if the background conditions are prohibitive to switch on the tracker system.

5 Calibration and Alignment

The final calibration and alignment of the VLQ spectrometer will be done in situ using QED Compton scattering events

$$e\,p \quad\rightarrow\quad e'\,\gamma\,p\ . \tag{9}$$

The cross section is rather large, of $\mathcal{O}(10\text{ nb})$, thus statistics will not be a serious problem. The basic idea is to exploit the energy conservation and the transverse energy balance between the final state lepton and photon

$$\begin{aligned} E'_e + E_\gamma &= E_e\ , & (10)\\ E'_e \sin\theta_e &= E_\gamma \sin\theta_\gamma\ . & (11)\end{aligned}$$

We denote the measured energy and the corresponding error of the clusters in the two calorimeter modules by E_1 and σ_1 and E_2 and σ_2. The energy conservation constraint eq. (10) can then be used to perform a χ^2 fit with

$$\chi^2 \;=\; \sum_{N_{evt}} \frac{(\kappa_1\,E_1 + \kappa_2\,E_2 - E_e)^2}{\sigma_1^2+\sigma_2^2}\ , \tag{12}$$

where κ_1 and κ_2 are the overall calibration factors of modules 1 and 2. The relative precision of the calibration constants is given by $\delta\kappa/\kappa = (\sigma_E/E_e)/\sqrt{N_{evt}} \simeq 3.5\cdot 10^{-2}/\sqrt{N_{evt}}$. Thus 1500 events are sufficient to get $\delta\kappa/\kappa \lesssim 10^{-3}$.

It is straightforward to extend the method to the calorimeter cells by replacing the measured cluster energy by

$$\kappa E \; = \; \sum_i C_i E_i \; ,$$

where the sum is taken over all calorimeter cells i used in the cluster reconstruction, having an energy deposition E_i and a calibration coefficient C_i.

The relative alignment of the calorimeter with respect to the VLQ tracking system can be achieved by using electrons or cosmic rays. The expected precision is given by the spatial resolution of the VLQ tracking system.

For the absolute alignment of the VLQ spectrometer it is intended to apply the double angle method. Using eqs. (10) and (11), the cluster energies can be expressed in terms of the polar angles θ_1 and θ_2 and the lepton beam energy E_e

$$E_1(\theta_1,\theta_2) \; = \; \frac{2\,E_e\,\sin\theta_2}{\sin\theta_1+\sin\theta_2-\sin(\theta_1+\theta_2)} \, , \tag{13}$$

$$E_2(\theta_1,\theta_2) \; = \; \frac{2\,E_e\,\sin\theta_1}{\sin\theta_1+\sin\theta_2-\sin(\theta_1+\theta_2)} \, . \tag{14}$$

For angles close to π one can approximate $\sin\theta = \sin(\pi-\theta) \simeq r/|z_{VLQ}-z_{vtx}|$, where $r = \sqrt{(x_0+x_{VLQ})^2+(y_0+y_{VLQ})^2}$ is the radial distance to the beam line, $(x_{VLQ},\ y_{VLQ},\ z_{VLQ})$ are the cluster coordinates and $(x_0,\ y_0)$ is the transverse offset of the calorimeter module. Rewriting eqs. (13) and (14) one gets

$$E_1(\theta_1,\theta_2) \; = \; E_e\,\frac{r_2}{r_1+r_2} \, , \tag{15}$$

$$E_2(\theta_1,\theta_2) \; = \; E_e\,\frac{r_1}{r_1+r_2} \, , \tag{16}$$

independent of the z vertex coordinate z_{vtx}.

Using the calibrated energies E_1^{cal} and E_2^{cal} as constraints one can minimize the χ^2 expression

$$\chi^2 \; = \; \sum_{N_{evt}} \left\{ \frac{(E_1^{cal}-E_1(\theta_1,\theta_2))^2}{\sigma_1^2} + \frac{(E_2^{cal}-E_2(\theta_1,\theta_2))^2}{\sigma_2^2} \right\} \tag{17}$$

and determine the relative positions of the two calorimeter modules with respect to each other as well as their absolute positions $(x_0,\ y_0)$, for which the vertex coordinates $(x_{vtx},\ y_{vtx})$, being regularly monitored on an run-by-run basis, need to be known.

A position accuracy of $\sigma_{x_0 y_0} \simeq 30\ \mu$m can be achieved with 1000 events. A misalignment by 50 μm causes a systematic shift of the scattering angle by $\delta\theta_{sys} \simeq 15\ \mu$rad. This has to be compared with the error of $\sigma_\theta \simeq 30\ \mu\text{rad}/\sqrt{N_{track}}$, if the the vertex reconstruction is included with a typical resolution of $\sigma_z \simeq 1\ \text{cm}/\sqrt{N_{track}}$ for N_{track} well measured long tracks.

Similar methods have been applied to align the BEMC [20], where a positioning error of 0.2 mm was obtained with 24 QED Compton scattering events.

6 Physics Performance

The kinematic variables are determined from the scattered lepton energy E_e' and the polar angle θ_e

$$Q^2 = 2\,E_e\,E_e'\,(1+\cos\theta_e)\,, \tag{18}$$

$$x = \frac{E_e}{E_p}\,\frac{E_e'\,(1+\cos\theta_e)}{2\,E_e - E_e'\,(1-\cos\theta_e)}\,, \tag{19}$$

$$y = 1 - \frac{E_e'\,(1-\cos\theta_e)}{2\,E_e}\,, \tag{20}$$

where E_e is the lepton beam energy and E_p is the proton beam energy. The kinematic variables are related by $Q^2 = x\,y\,s$.

The resolutions on Q^2 and x (in the small angle $\pi - \theta_e$ approximation)

$$\frac{\delta Q^2}{Q^2} = 2\,\frac{\delta\theta_e}{\pi-\theta_e} \oplus \frac{\delta E_e'}{E_e'}\,, \tag{21}$$

$$\begin{aligned} \frac{\delta x}{x} &= 2\,\frac{\delta\theta_e}{\pi-\theta_e} \oplus \frac{1}{y}\,\frac{\delta E_e'}{E_e'} \\ &= 2\,\frac{\delta\theta_e}{\pi-\theta_e} \oplus \frac{E_e}{E_e - E_e'}\,\frac{\delta E_e'}{E_e'} \end{aligned} \tag{22}$$

are dominated by the energy measurement, provided the lepton direction can be determined with a spatial resolution of better than $\sigma_{xy} \lesssim 100$ μm. The divergence in the x resolution at low y can be avoided by introducing a cut on the y variable with a typical value of $y \gtrsim 0.1$.

The performance of the proposed VLQ spectrometer has been studied by generating DIS events [21] using the interpolated parton densities of GRV LO [1] and DL [2], as described in section 2. Reliable parton density estimates don't yet exist in the kinematic $x - Q^2$ range of interest, but this approximation is completely adequate for the study of acceptance, resolution and migration effects. For the time being QED radiation has been neglected. The event simulation is based on four-vectors smeared according to the experimental resolutions and acceptances, including the z vertex distribution. Multiple scattering in the beam pipe and the two VLQ tracking planes is taken into account.

The event selection is similar to the standard DIS analysis and requires the following conditions:

1. The scattered lepton has to be well detected within the VLQ acceptance, i.e. within a fiducial volume 0.5 cm away form the borders of the calorimeter.

2. The energy of the scattered lepton has to exceed $E_e' > 4$ GeV.

3. The energy–longitudinal momentum conservation $|\sum(E - p_z) - 2\,E_e| < 10$ GeV must be satisfied, where the sum extends over all detected particles or energy clusters.

4. The scaling variable y has to fulfill $0.15 < y < 0.80$, and y_h as measured from the hadronic energy flow has to exceed $y_h > 0.15$.

Requirements (1) and (2) assure that the kinematic variables are well measured. The lepton scattering angle is taken from the VLQ tracking system, assuming that the primary interaction vertex can be well determined. Requirement (3) provides a good containment of the final state particles. The low y and y_h cuts in requirement (4) ensure a consistent measurement and remove the divergent behaviour of the x resolution at low y values. The high y cut is introduced to avoid the region affected by large radiative corrections.

The current quark jet, being also emitted in the backward direction, carries in general little energy and is not expected to produce an additional cluster in the VLQ, which could mimic a lepton. Background from photoproduction events with a misidentified lepton can be essentially eliminated by the cuts (3) and (4). The remaining beam-gas scattering background can be effectively reduced by measuring the z position of the vertex with the VLQ and/or central tracking system. This background can also be subtracted on a statistical basis using e pilot bunches.

The expected rate is $\sim 20,000$ accepted events for $\mathcal{L} = 0.1\ pb^{-1}$.

The polar angle acceptance of the VLQ calorimeter around $\phi = \pm 90°$ is uniform over the range $177.3° < \theta_e < 179.4°$. The geometrical azimuthal acceptance is 40%. Experience will show, whether it will become feasible to extend the calorimeter acceptance closer to the beam pipe, thereby gaining in event statistics at the expense of a slightly worse lepton energy resolution at the lower edge of the calorimeter.

The accessible $x - Q^2$ region of the VLQ spectrometer is shown in figure 1. It covers the kinematic range $0.03\ \mathrm{GeV}^2 \lesssim \mathrm{Q}^2 \lesssim 0.7\ \mathrm{GeV}^2$ and $5 \cdot 10^{-7} \lesssim x \lesssim 5 \cdot 10^{-5}$. Also indicated is the SPACAL acceptance, which comfortably matches the VLQ measurement. The small gap between both calorimeters may be closed by dedicated shifted vertex runs with either $z_{vtx} \simeq +70$ cm (lower Q^2 reachable in the SPACAL) or $z_{vtx} \simeq -70$ cm (higher Q^2 reachable in the VLQ), see figure 37.

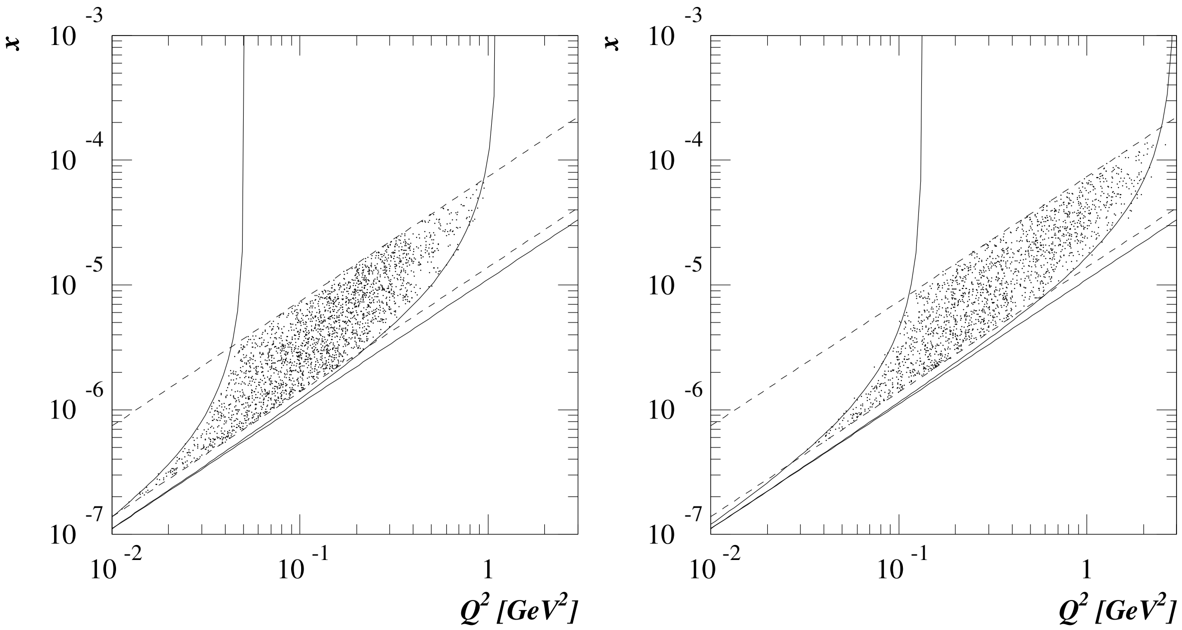

Figure 37: The accessible phase space of the VLQ detector with the collision vertex shifted towards $\langle z_{vtx} \rangle = +70$ cm (left) and $\langle z_{vtx} \rangle = -70$ cm (right)

The expected resolutions in the kinematic variables Q^2 and x, as derived from a comparison of reconstructed and generated quantities, are shown in figure 38. Both resolutions exhibit a rather constant behaviour over the whole accepted phase space with average values of

$$\begin{aligned} \left\langle \delta Q^2/Q^2 \right\rangle &= 4.4\ \% , \\ \langle \delta x/x \rangle &= 11.5\ \% . \end{aligned}$$

This performance allows the use of a very fine binning in the $F_2(x, Q^2)$ analysis, keeping migration effects small.

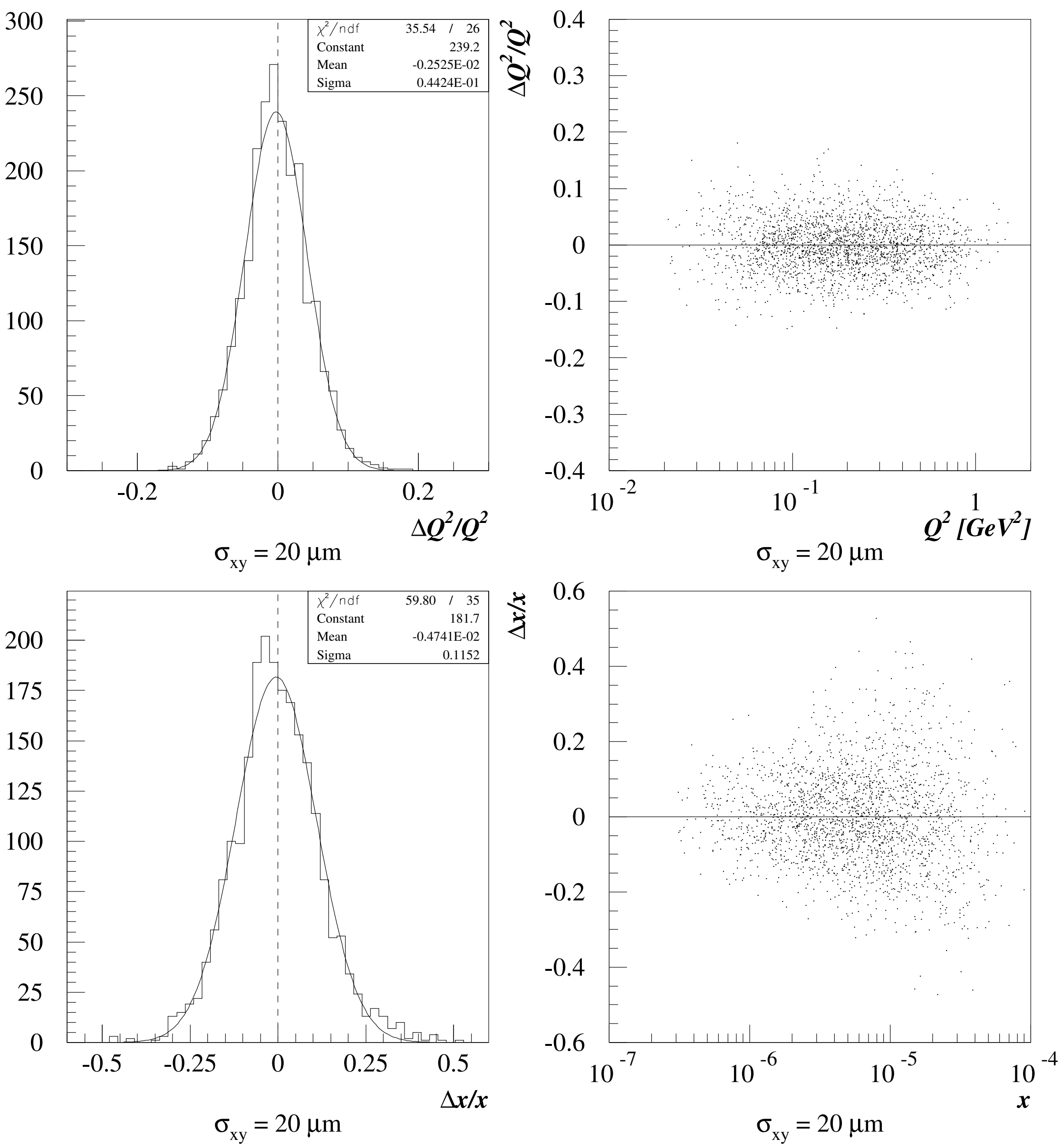

Figure 38: Resolutions of the kinematic variables $\Delta Q^2/Q^2$ (upper figures) and $\Delta x/x$ (lower figures), assuming a VLQ tracking resolution of $\sigma_{xy} = 20\ \mu$m

If the lepton direction would be measured by the VLQ calorimeter alone, the Q^2 resolution would be worse by a factor of ~ 1.5, the degradation in the x resolution is less severe (~ 1.1). The gain in the Q^2 and x resolutions levels off for spatial resolutions better than $\sigma_{xy} \lesssim 100\ \mu m$. However, a precise VLQ tracking of the scattered lepton offers the important possibility to have an independent measurement of the interaction vertex and thereby allows the identification very low Q^2 DIS events in a purely inclusive analysis, without any bias from additional detector elements. It further provides another handle to reject off-vertex background.

The expected z vertex resolution obtained with two VLQ tracking planes is displayed in figure 39. The resolution deteriorates rapidly for tracks close to the beam line, due to the very small angles of incidence with respect to the normal to the detector planes. The average z vertex resolution is $\langle \Delta z_{vtx} \rangle \simeq 10.6$ cm, which has to be compared to the rms width of $\sigma_z \simeq 12$ cm of the vertex distribution given by the HERA beams. The z vertex resolution is close to the limit given by multiple scattering in the beam pipe, see figure 40. A tracking performance of $\sigma_{xy} = 100\ \mu$m, which may be sufficient for the determination of the kinematics, would not provide any useful vertex reconstruction. The situation would slightly improve if it were possible to further separate the two VLQ tracking planes.

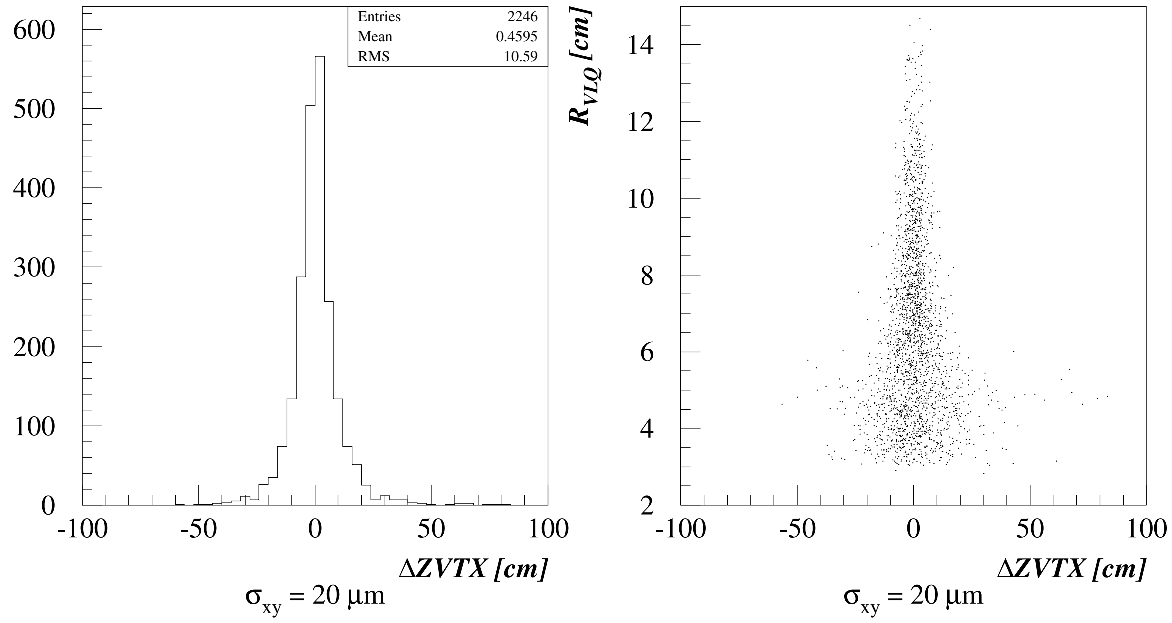

Figure 39: Expected z vertex resolution Δz_{vtx} from the VLQ tracking system. The degradation around a radial distance of $R_{VLQ} \simeq 5$ cm is due to multiple scattering in the beam pipe (right plot).

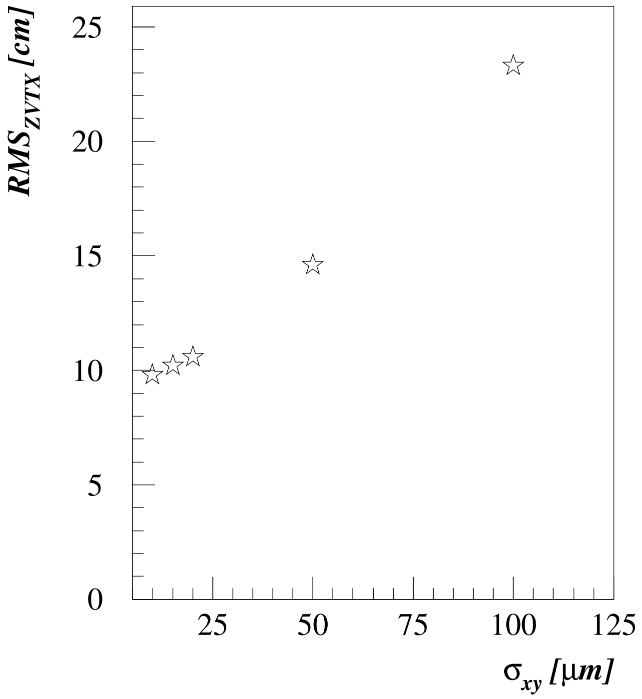

Figure 40: Expected z vertex resolution $rms\ z_{vtx}$ for various assumptions on the VLQ tracking performance σ_{xy}

7 Finances, Responsibilities and Schedule

The responsibilities in building the VLQ detector, the new beam pipe and modifying the existing beam pipe are shared as follows:

Carbon fiber and Al beam pipes	Aachen 1
Stainless steel beam pipe and incorporation of beam pickup antenna into compensator	DESY
Moving mechanics	Aachen 1, DESY
Tracking system	Aachen 1
Calorimeter mechanics and electronics	Heidelberg IHEP
Calorimeter trigger	Košice
ToF system	Košice, Praha
Infrastructure	DESY

A breakdown of the necessary investments is shown in table 5. Costs for technical manpower in the institutes, for prototyping and for contingency are not included. The sharing of the costs is given in table 6.

We plan to install the new beam pipes and the complete detector during the shut down in early 1997. The detectors will be assembled above ground and will be installed as a whole.

It is planned to construct the calorimeter during 1996. Both modules will be ready by November. They will be calibrated with a stand-alone electronics setup at the DESY synchrotron during the second half of November.

Prototypes of the micro-strip detectors (made from 2–inch wafers) will be ready by the end of April 1996 and tested in a beam at CERN, using the premux128 preamplifier chip developed for CMS. The test will include measurements in a magnetic field. At the same time a laboratory test of a GaAs detector will be performed using the APC chip and readout with an OnSiRoc controller. All micro-strip detectors will be ready by the end of 1996. For the final tests, to be done early 1997 in a laboratory test stand, it is crucial that the electronics (tested APC's, hybrids, controllers) are available by the end of 1996.

Item	kDM
General	
Beam-pickup into Compensator	30
Beampipe (SS)	10
Beampipe (CFK)	40
Beampipe (Al)	10
Moving Mechanics	30
Subtotal	120
Tracking System	
Detectors and Support	15
Front-end Electronics (Hybrids, APC)	50
Readout (Repeater, OnSiRoc, Buffer)	40
Cables	10
Subtotal	115
Calorimeter	
Mechanics (Material, Support)	41
Electronics (Front-end + Readout)	55
Trigger	15
Photodiodes	50
Optics (Scintillator, WLS)	18
Subtotal	179
TOF	
Phototubes, Mechanics, Scintillators	6
DAQ, Slow Control	
Slow control and VLQ monitoring	10
Grand Total	430

Table 5: Project investments

	Aachen 1 kDM	DESY kDM	Heidelberg kDM	Praha kDM	NN kDM	Total kDM
General	25		55		40	
Tracking	70	45				
Calorimeter			179			
TOF				6		
DAQ, Slow Control	5		5			
	100	45	239	6	40	430

Table 6: Sharing of costs

References

[1] M. Glück, E. Reya and A. Vogt, Z. Phys. C53 (1992) 127;
M. Glück, E. Reya and A. Vogt, Z. Phys. C67 (1995) 433.

[2] A. Donnachie and P.V. Landshoff, Phys. Lett. B296 (1992) 227.

[3] H. Abramowicz et al., Phys. Lett. B269 (1991) 465.

[4] H1 Collaboration, S. Aid et al., preprint DESY 96-039 (1996).

[5] H1 Collaboration, S. Aid et al., preprint DESY 96-023 (1996).

[6] T. Uematsu and T. Walsh, Nucl. Phys. B199 (1982) 93.

[7] M. Drees and R.M. Godbole, preprint MADPH-95-891, LNF-95/027 (1995).

[8] D. Graudenz and G. Veneziano, preprint CERN-TH 95-232 (1995).

[9] Optectron Industries, Technical Data Sheet

[10] T. Beckmann and A. Hölscher, Internal Note ASIC Laboratory Heidelberg HD-ASIC-14-0196, *'Test of HELIX 1.1'*.

[11] H1 BEMC Group, preprint DESY 95-177 (1995), *'The H1 Backward Calorimeter BEMC and its Inclusive Electron Trigger'*.

[12] GEANT manual, CERN program library.

[13] HAMAMATSU Photonics, Technical Data Sheet.

[14] W. Braunschweig et al., Nucl. Phys. B (Proc. Suppl.) 44 (1995) 391, *'Charge Collection Efficiencies and Reverse Current Densities of GaAs Detectors'*.

[15] Freiberger Elektronikwerkstoffe, 09599 Freiberg, Germany

[16] W.Braunschweig et al., Nucl. Instr. & Meth. A372 (1996) 111, *'Investigation of the radiation damage of GaAs detectors by neutrons and photons'*.

[17] J.Bürger et al., preprint DESY 95-049 (1995), *'The Readout System of the New H1 Silicon Detectors'*;
H1 Collaboration, PRC 92/01 and internal note H1 06/92-226 (1992), *'Technical Proposal to build Silicon Tracking Detectors for H1'*.

[18] W. Braunschweig et al., Nucl. Instr. & Meth. A370 (1996) 377, *'Measurement on a GaAs Microstrip Detector with 50 GeV/c Electrons'*.

[19] H1 Collaboration, I. Abt et al., DESY internal report H1-96/01 (1996), *'The H1 Detector at HERA'*.

[20] A. Courau and S. Kermiche, internal note H1-12/92-260 (1992);
S. Kermiche, PhD Thesis, LAL 94-14 (1994), Orsay.

[21] H.-U. Martyn, internal note H1-12/94-416 (1994), *'CIMODEL'*.

Contents

List of Figures

List of Tables